Chapter 5

Stray-Light Correction of the Marine Optical Buoy

Steven W. Brown[1], B. Carol Johnson[1], Stephanie J. Flora[2], Michael E. Feinholz[2], Mark A. Yarbrough[2], Robert A. Barnes[3], Yong Sung Kim[4], Keith R. Lykke[1], and Dennis K. Clark[5]

[1]*Optical Technology Division, National Institute of Standards and Technology, Gaithersburg, Maryland*
[2]*Moss Landing Marine Laboratories, Moss Landing, California*
[3]*Science Applications International Corporation, Beltsville, Maryland*
[4] *Data Systems Technologies, Inc., Rockville, Maryland*
[5]*National Oceanic and Atmospheric Administration, National Environmental Satellite Data and Information Service, Camp Springs, Maryland*

5.1 INTRODUCTION

In ocean-color remote sensing, approximately 90 % of the flux at the sensor originates from atmospheric scattering, with the water-leaving radiance contributing the remaining 10 % of the total flux. Consequently, errors in the measured top-of-the atmosphere radiance are magnified a factor of 10 in the determination of water-leaving radiance. Proper characterization of the atmosphere is thus a critical part of the analysis of ocean-color remote sensing data. It has always been necessary to calibrate the ocean-color satellite sensor vicariously, using *in situ*, ground-based results, independent of the status of the pre-flight radiometric calibration or the utility of on-board calibration strategies (Gordon 1998). Because the atmosphere contributes significantly to the measured flux at the instrument sensor, both the instrument and the atmospheric correction algorithm are simultaneously calibrated vicariously.

The Marine Optical Buoy (MOBY) (Clark *et al*. 1997; Clark *et al*. 2002a; Clark *et al*. 2002b), deployed in support of the Earth Observing System (EOS) since 1996, serves as the primary calibration station for a variety of ocean-color satellite instruments, including the Sea-viewing Wide Field-of-view Sensor (SeaWiFS) (Barnes *et al*. 2000), the Moderate Resolution Imaging Spectroradiometer (MODIS) (Esaias *et al*. 1998), the Japanese Ocean Color Temperature Scanner (OCTS) (Isaacman *et al*. 1999), and the French Polarization and Directionality of the Earth's Reflectances (POLDER) (Deschamps *et al*. 1994). MOBY is located off the coast of Lanai, Hawaii. The site was selected to simplify the application of the atmospheric correction algorithms (Clark *et al*. 1997). Vicarious calibration using MOBY data allows for a thorough comparison and merger of ocean-color data from these multiple sensors (Wang *et al*. 2002).

MOBY uses an instrument known as the Marine Optical System (MOS) to detect radiation over the spectral range from 350 nm to 955 nm. The MOS system contains two single-grating spectrographs, a blue spectrograph (BSG) to measure light in the near ultraviolet and visible from 340 nm to 640 nm and a red spectrograph (RSG) to measure light in the red and near infrared from 550 nm to 955 nm (Clark *et al*. 2002a; Clark *et al*. 2002b). MOS resides in the MOBY instrument bay located at the bottom of the buoy. It is connected by optical fibers to radiance and irradiance ports on the three MOBY arms (denoted Top, Mid, and Bot), located at different ocean depths (typically 1.5 m, 5 m and 9 m), as well as to a surface irradiance port. MOBY measures upwelling radiance, L_u, as well as the down-welling irradiance, E_d. A fiber-optic multiplexer in the MOBY instrument bay selects which spectrum is acquired by MOS. As described in Clark *et al*. (2002b), these data are used to determine the water-leaving radiance, L_w.

MOBY buoys are typically deployed for 3 months to 4 months, then retrieved for servicing and repair. Deployments are numbered sequentially. One MOS instrument, MOS204, is used for even-buoy deployments while a separate instrument, MOS205, is used for odd deployments. The buoys are calibrated before and after deployment using sources traceable to radiometric standards maintained at the National Institute of Standards and Technology (NIST) (Clark *et al*. 2002a). During a deployment, the buoy's radiometric stability is checked using on-board

calibration sources and monthly lamp calibrations by divers (Clark *et al*. 2002a). The MOBY radiometric standards are monitored during the year using two single-channel filter radiometers, called Standard Lamp Monitor (SLM) radiometers, with filter channels at 412 nm and 870 nm. They are calibrated at NIST on a regular basis. In addition, transfer-standard artifacts are deployed from NIST to the MOBY field laboratory on a yearly basis to validate the calibration protocols and assess the accuracy and stability of the MOBY spectral radiance sources.

The generally stated uncertainty goal for ocean-color radiometry is 5 % ($k = 1$) for L_w, which results in an uncertainty of 35 % for chlorophyll-*a* (Hooker *et al*. 1993). This requirement for high accuracy places stringent demands on the uncertainties in water-leaving radiance measurements with MOBY. The uncertainties of MOBY measurements of water-leaving radiance L_w — without accounting for the effects of stray light — are estimated to be in the range from 4 % to 8 % ($k = 1$) (Clark *et al*. 2002a).

Spectrographs are imaging systems with dispersive elements and multi-element detectors that enable simultaneous acquisition of an entire spectrum over some finite spectral width. There are intrinsic limitations in the background signal originating from radiation scattered from imperfections in the optical elements in the instrument. This unwanted background radiation, called stray light, while small — on the order of 0.01 % or less of the incident spectral radiance in a single grating spectrograph — can give rise to unforeseen errors, often much larger than anticipated, when the spectral distribution of a source being measured differs significantly from the spectral distribution of the calibration source. Such a situation is routinely encountered in oceanographic measurements, where instruments are calibrated against incandescent sources with a peak radiance in the short-wave infrared (~1000 nm) and subsequently measure the radiance of the ocean, which peaks in the blue spectral region (~450 nm) (Fig. 5.1). Consequently, stray light, if not properly accounted for, can have a significant effect in ocean-color research (Clark *et al*. 2002a).

Measurements with the two spectrographs in the MOS systems can be compared in the spectral interval from about 580 nm to 630 nm. In this spectral range the two spectrographs give different values for L_u or E_d at a common wavelength. In Fig. 5.2, L_u is shown for the Top (Top), Middle (Mid) and Bottom (Bot) MOBY arms. The difference in the measured radiance in the overlap region is a function of depth, increasing for deeper-lying MOBY arms. While the signal is small in this region (approximately 1 % of the peak radiance), the lack of agreement in the overlap region and particularly its dependence on the spectral distribution of the upwelling radiance are possible manifestations of stray light in the system.

To look for stray light in MOS, the response of the two spectrographs in the MOS205 system to monochromatic laser excitation was measured. In this experiment, lasers were directed into an integrating sphere and the radiance was measured with each MOBY arm. For monochromatic radiation, the entrance slit is spatially imaged on the detector. Ideally, no radiation falls on detector elements outside the image. In practice, the image is modified by scattered light within the spectrograph and every element in the array can in principle have a finite response to this monochromatic radiation. Results for the two spectrographs are shown in Fig. 5.3. The spectra are similar for both spectrographs. There are three components to the image: a strong, sharp peak corresponding to the image of the spectrograph entrance slit on the CCD; a broad, peaked structure around the slit image; and a non-zero constant component. These three components are similar to specular, haze and diffuse components of reflectance. The specular component corresponds to the properly imaged radiation; the haze and diffuse components arise from light scattered in the spectrograph, principally from the grating. These two components are analogous to the spectral out-of-band features commonly observed in a filter radiometer.

In certain spectral regions, additional features are observed in the CCD response. From physical examination of the spectrographs, the additional peaks are associated with a higher order diffraction peak from the grating. Optical ray-trace modeling of the system confirms this hypothesis. Representative MOBY images showing this reflection peak in the system response are given in Fig. 5.4. Note, for example, the secondary reflection peak centered about pixel 160 (pixel 725) for light imaged onto pixel 195 (pixel 760) for the BSG (RSG).

This scattered light causes unknown but potentially significant errors in the measured up-welling radiance. Consequently, the MOS instrument was characterized for its stray-light response and the results incorporated into an algorithm that was developed to correct its measurements for stray light. In Section 5.2, we describe the iterative approach used to correct a MOS spectrum for stray light. The derivation of the instrument's stray-light parameters is described in Section 5.3 and applied to MOBY data sets in Section 5.4.
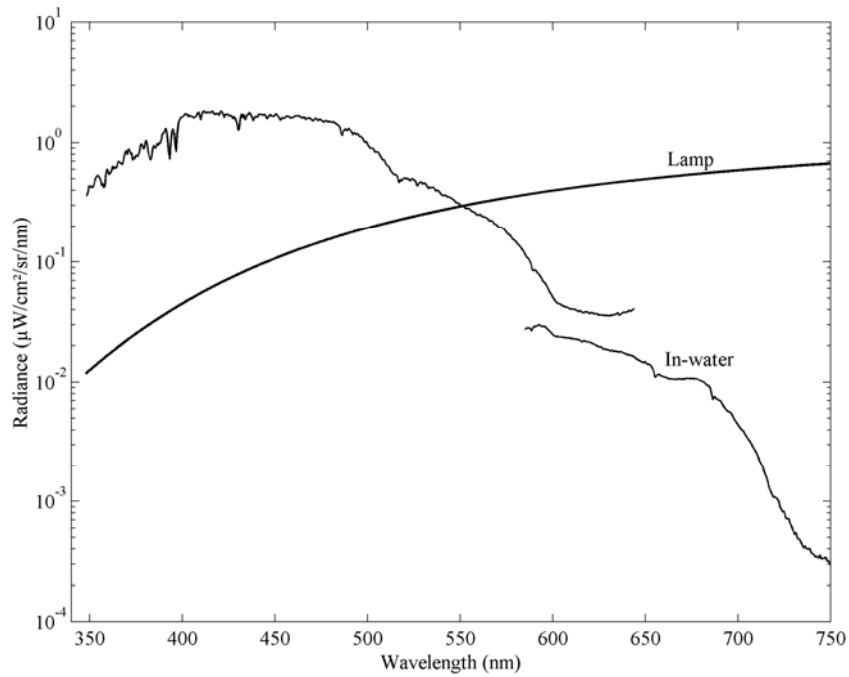
Figure 5.1. Typical spectral radiances of a lamp-based calibration source and in-water, up-welling radiance at the MOBY site.
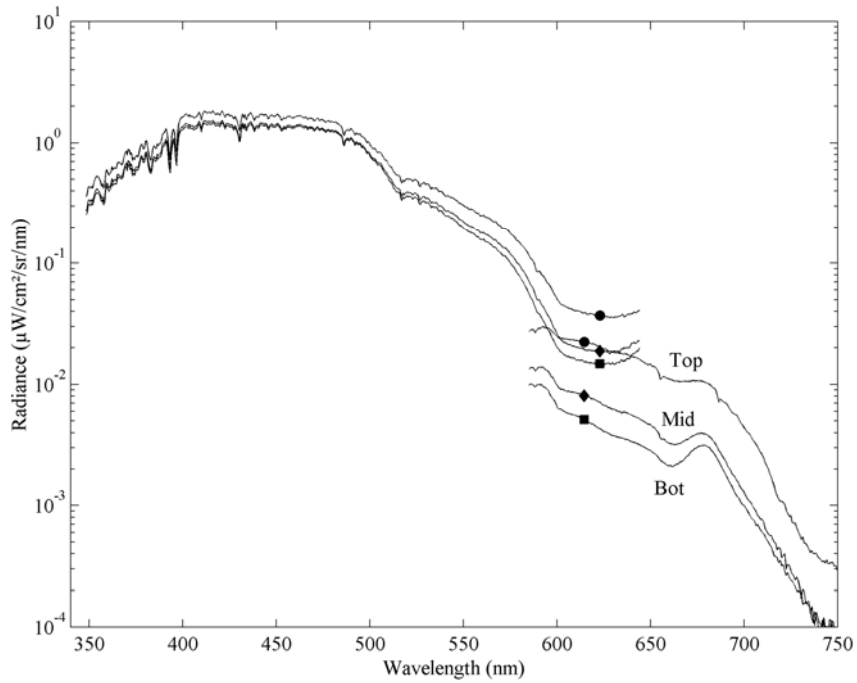

Figure 5.2. MOBY L_u (typical) for the three MOBY arms showing the lack of agreement in the overlap region where both spectrographs make measurements.
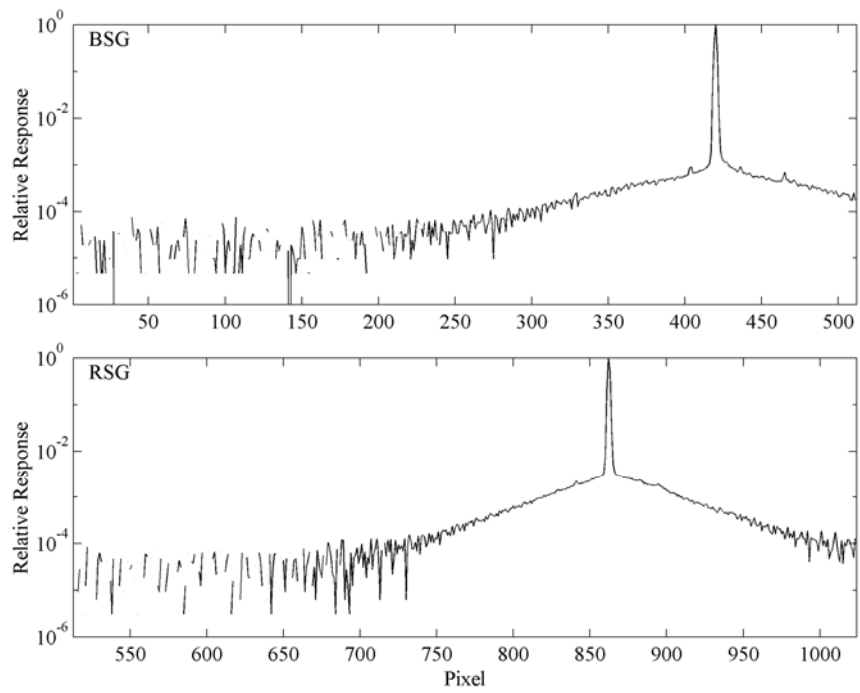
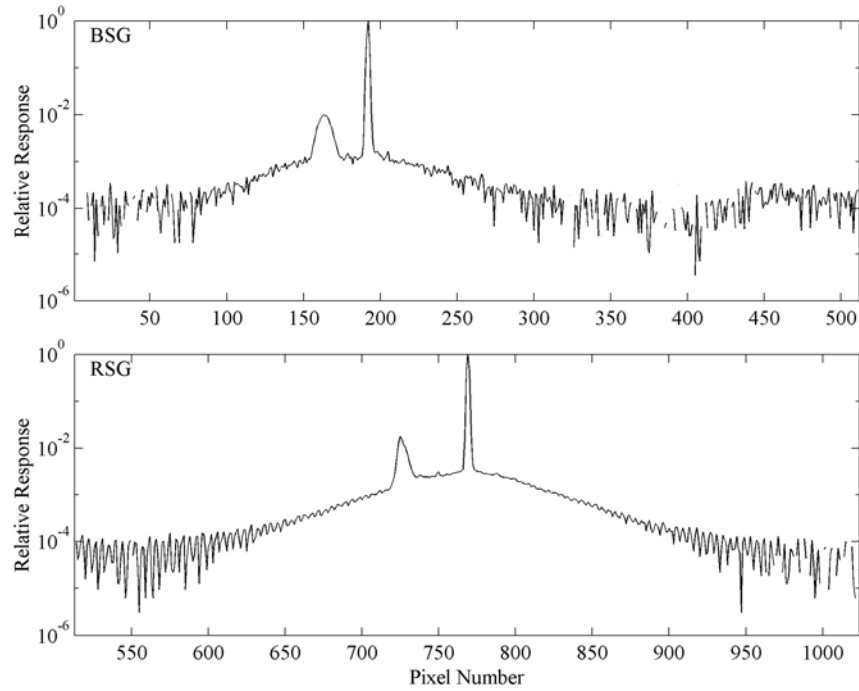Figure 5.3. MOS205 response to monochromatic excitation.

Figure 5.4. MOS205 response to monochromatic excitation showing reflection peaks.

5.2 STRAY-LIGHT CORRECTION ALGORITHM

Each MOS spectrograph uses a 512 by 512 element CCD array to detect incident radiation. When acquiring an image, the signals from the central 384 pixels in each column are averaged and a 512-element array is generated from each spectrograph. The total signal from element i of a MOS CCD is given by the equation

$$S_i = \int r_i(\lambda) L(\lambda) d\lambda \tag{5.1}$$

where $r_i(\lambda)$ is the spectral responsivity of element i and $L(\lambda)$ is the spectral radiance of the source being measured. Note that $r_i(\lambda)$ is the spectral responsivity of element i when considered as part of the spectrograph and includes effects such as grating diffraction efficiency and mirror losses.

For monochromatic radiation, an image of the entrance slit is formed on the detector. Expressed as a function of wavelength rather than array element, this normalized spatial image function is known as the instrument's slit-scatter function $\sigma_i(\lambda_i - \lambda)$ (Kostkowski 1979), with the 'exit slit' in this case determined by the array element's spatial width and λ_i is the wavelength of element i's maximum responsivity. There is a fixed relationship between the excitation wavelength and the position of the image on the array. As the wavelength changes, the spatial image moves across the array.

Knowing this relationship enables us to determine the fraction of incident light at some wavelength that is scattered onto a particular element. For example, for the wavelength λ_{ex} in Fig. 5.3, 0.01 % of the light imaged on element 420 (BSG) is scattered onto element 300. Assuming each element in the detector array has the same average spectral responsivity, the signal from element 300 to radiation at wavelength λ_{ex} is 0.01 % of the signal from element 420.

Following Kostkowski (Kostkowski 1979), the total responsivity of element i can be approximated by the product of the slit-scattering function and the maximum responsivity of each array element $\bar{r}_i(\lambda_i)$ (Fig. 5.5)

$$r_i(\lambda) = \overline{r_i}(\lambda_i)\sigma_i(\lambda_i - \lambda). \tag{5.2}$$

Knowing the slit-scatter function, we have a set of 512 coupled equations

$$S_i = \overline{r_i}(\lambda_i)\int\sigma_i(\lambda_i - \lambda)L(\lambda)d\lambda \tag{5.3}$$

that can be directly solved for either $\overline{r_i}(\lambda_i)$ or $L(\lambda)$ (provided the other variable is known) using a generalized least-squares approach (Shumaker 1979). Approximate inverse solutions using Singular-Value-Decomposition (SVD) of the applicable matrices are robust and should be directly applicable to this system (Mueller 2002). We used a simpler, more intuitive, iterative approach utilizing the inherently discrete nature of the CCD response. Separating Eq. (5.1) into an in-band (*ib*) and an out-of-band (*oob*) component and assuming that the source radiance is approximately constant over the in-band spectral width, Eq. (5.1) can be written as

$$S_i = \int_{ib} r_i(\lambda)L(\lambda)d\lambda + \int_{oob} r_i(\lambda)L(\lambda)d\lambda = L(\lambda_i)R_i(\lambda_i) + \overline{r_i}(\lambda_i)\int_{oob}\sigma_i(\lambda_i - \lambda)L(\lambda)d\lambda, \tag{5.4}$$

where λ_i is the wavelength corresponding to the peak responsivity of element i, $L(\lambda_i)$ is the source radiance at λ_i, and $R_i(\lambda_i)$ is the integrated in-band responsivity of element i

$$R_i(\lambda_i) = \overline{r_i}(\lambda_i)\int_{ib}\sigma_i(\lambda_i - \lambda)d\lambda. \tag{5.5}$$

Measuring a calibration source of known spectral radiance, $L_c(\lambda)$, and solving for $R_i(\lambda_i)$ in Eq. (5.4), the integrated in-band responsivity of pixel i can be written

$$R_i(\lambda_i) = \frac{S_i}{L_c(\lambda_i)} - \frac{\overline{r_i}(\lambda_i)}{L_c(\lambda_i)}\int_{oob}\sigma_i(\lambda_i - \lambda)L_c(\lambda)d\lambda. \tag{5.6}$$

The second term on the right hand side of Eq. (5.6) is the stray-light contribution to the total responsivity. Utilizing the discrete nature of the spectrograph detector array and substituting Eq. (5.5) for $\overline{r_i}(\lambda_i)$, a recursion relation is developed for $R_i(\lambda_i)$

$$R_i^{(n)}(\lambda_i) = \frac{S_i}{L_c(\lambda_i)} - \frac{1}{L_c(\lambda_i)\int_{ib}\sigma_i(\lambda_i - \lambda)d\lambda}\sum_{oob}R_j^{(n-1)}(\lambda_j)\sigma_i(\lambda_i - \lambda_j)L_c(\lambda_j)\Delta\lambda, \tag{5.7}$$

where $\Delta\lambda$ is the pixel-to-pixel wavelength spacing and j extends over all 512 elements of the array. The original input values to the responsivity are the signals divided by the radiance of the calibration source

$$R_i^{(0)}(\lambda_i) = \frac{S_i}{L_c(\lambda_i)}. \tag{5.8}$$

Following the above discussion, the radiance of a source with an unknown spectral distribution can also be corrected for stray light. In this case, the relation is given by the expression

$$L^{(n)}(\lambda_i) = \frac{S_i}{R_i(\lambda_i)} - \frac{1}{R_i(\lambda_i)\int_{ib}\sigma_i(\lambda_i - \lambda)d\lambda}\cdot\sum_{oob}R_j(\lambda_j)\sigma_i(\lambda_i - \lambda_j)L^{(n-1)}(\lambda_j)\Delta\lambda, \tag{5.9}$$

where

$$L^{(0)}(\lambda_i) = \frac{S_i}{R_i(\lambda_i)}. \tag{5.10}$$

Note that the stray-light corrected responsivity must be used. A stable solution, with changes less than 0.1 %, is reached after 4 to 5 iterations. The solution is robust and insensitive to small variations in the input parameters.
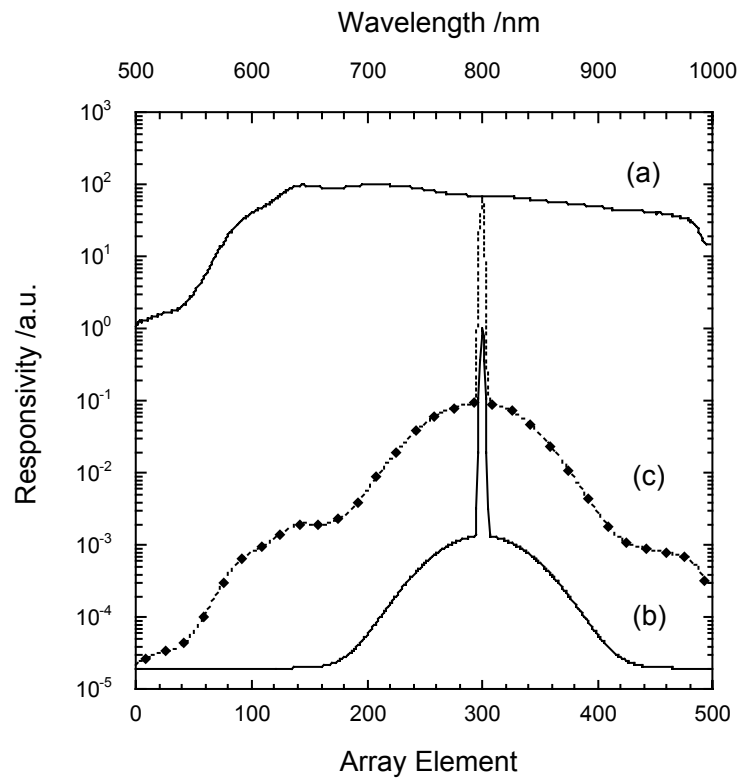
Figure 5.5. **(a)** A spectrograph's absolute spectral responsivity, $\bar{r}(\lambda)$. **(b)** Slit-scatter function for element 300, $\sigma_{300}(\lambda_{300} - \lambda)$. **(c)** Absolute spectral responsivity of element 300.

5.3 DERIVATION OF MOBY SLC MODEL PARAMETERS

There are a total of 3 MOS instruments actively used by the MOBY project. MOS202 is a stand-alone system, known as the MOS Profiler. It is a ship-board instrument used for bio-optical algorithm development and validation and is not directly associated with the MOBY buoy. MOS204 is used as the sensor in even-buoy MOBY deployments; MOS205 is used in odd-buoy deployments. In principle, model slit-scatter parameters need to be independently developed for each MOS and for each MOBY deployment, with separate factors for each MOBY arm, each port (E_d or L_u), for the top E_s port and for the bottom MOS port.

Examination of the system response to monochromatic excitation showed that the different arms (both E and L) within an individual buoy had the same slit-scatter function. The normalized responses of the MOBY top, middle and bottom arms with MOS205 to monochromatic excitation are shown in Figs. 5.6 and 5.7. Measurements also confirmed that the slit-scatter function remained the same before and after deployment for a particular buoy as well as from buoy to buoy for a particular MOS system. However, the slit-scatter function differs between MOS instruments (Fig. 5.8). Therefore, we only needed to derive model slit-scatter function parameters for a single port on a single MOBY arm for a particular MOS. The results were then extended to every MOBY arm, both L_u and E_d ports, and the E_s collector for a particular MOS system. Radiation entering the MOS directly from the bottom radiance port is imaged differently (Fig. 5.9) onto the CCD array. Consequently, the slit-scatter function parameters for the bottom MOS port on MOBY are considered separately and are not addressed in this work.

Experimental

In a spectroradiometer equipped with a single element detector, the dispersive element, *e.g.* the grating, is rotated while the detector is fixed. The center wavelength of the radiation imaged on the exit slit is a function of the angle of rotation of the grating. The instrument's slit-scatter function can be determined using a single fixed wavelength source and changing the wavelength of the radiation centered on the exit slit by rotating the grating in small steps.

In a spectrograph, the grating is fixed and the spectral selection determined by the image of the entrance slit onto a reference plane where the multi-element sensor is placed as well as the size of the individual elements in the sensor array. In this case, if we want to determine the system's spectral response over some finite spectral range, we need a tunable, monochromatic excitation system. NIST recently established a tunable-laser-based radiometric calibration facility for Spectral Irradiance and Radiance responsivity Calibrations using Uniform Sources, known as SIRCUS (Brown *et al*. 2000). In the SIRCUS facility, tunable, monochromatic, high-power lasers are fiber coupled into an integrating sphere, producing a nearly Lambertian, monochromatic source that overfills the entrance pupil of imaging systems such as MOS. The radiance of the source is determined at any wavelength by an irradiance standard detector, which is in turn directly traceable to primary radiometric standards maintained at NIST. A bench prototype of the MOS system was characterized and calibrated in this facility (Habauzit *et al*. 2003). The results demonstrated the validity of the stray-light correction approach.

The imaging onto the MOS CCDs in MOBY is slightly different than in the MOS system itself (Fig. 5.9). Consequently, a piece-wise characterization approach would not work and the entire MOBY system had to be characterized. Because of the logistical problems associated with transporting an object as large as MOBY to NIST and to the SIRCUS facility, as well as time constraints imposed by the operational protocols developed for MOBY, it was necessary to characterize and calibrate the buoys *in situ* at the calibration facility at the University of Hawaii Marine Center, Honolulu, Hawaii.

A fiber-coupled, laser-based integrating sphere source (ISS), similar to the radiance source in the SIRCUS facility, was developed for use at the MOBY field site. The system consisted of a 532 nm Nd:Vanadate laser pumping a Ti:sapphire laser for tunable radiation from 700 nm to 1000 nm or a dye laser with Rhodamine6G dye for tunable radiation from 565 nm to 615 nm. The Ti:sapphire laser was modified to enable intra-cavity doubling with doubled output from 410 nm to 440 nm. An etalon was placed in the laser cavity to ensure that the output was narrow-band (<0.01 nm). Fixed-frequency HeNe, Argon ion, and diode lasers were used for additional characterization at discrete wavelengths.
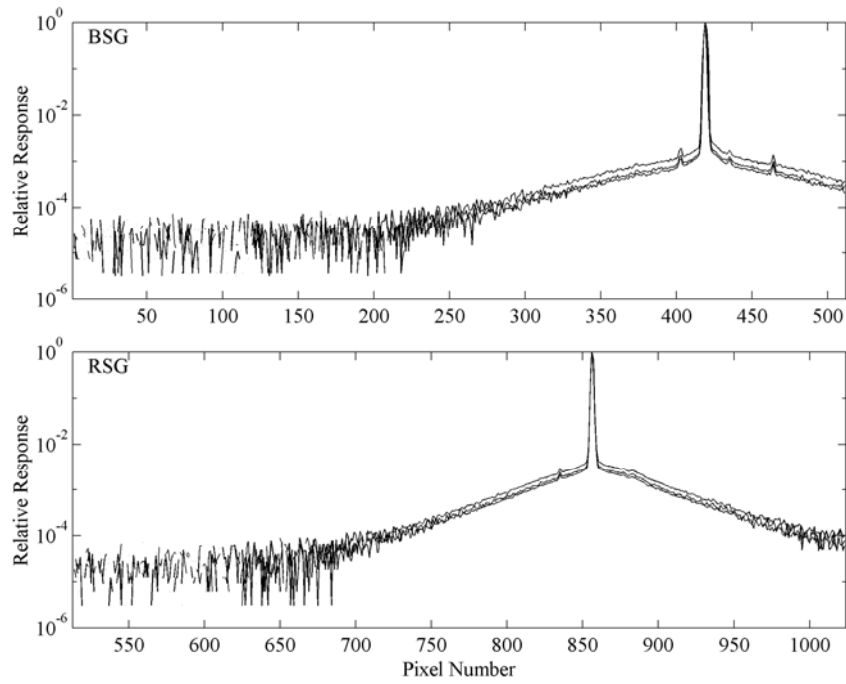
Figure 5.6. Normalized MOS205 response to monochromatic excitation from the top, middle and bottom arms (radiance collector) of MOBY219.
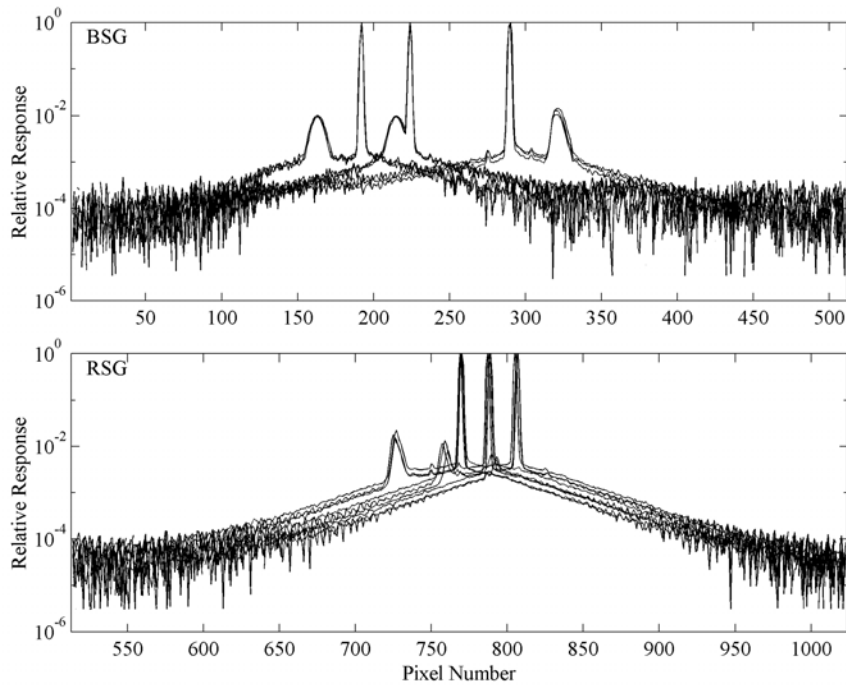

Figure 5.7 Normalized MOS205/MOBY219 response to monochromatic excitation from the three arms showing reflection peaks.
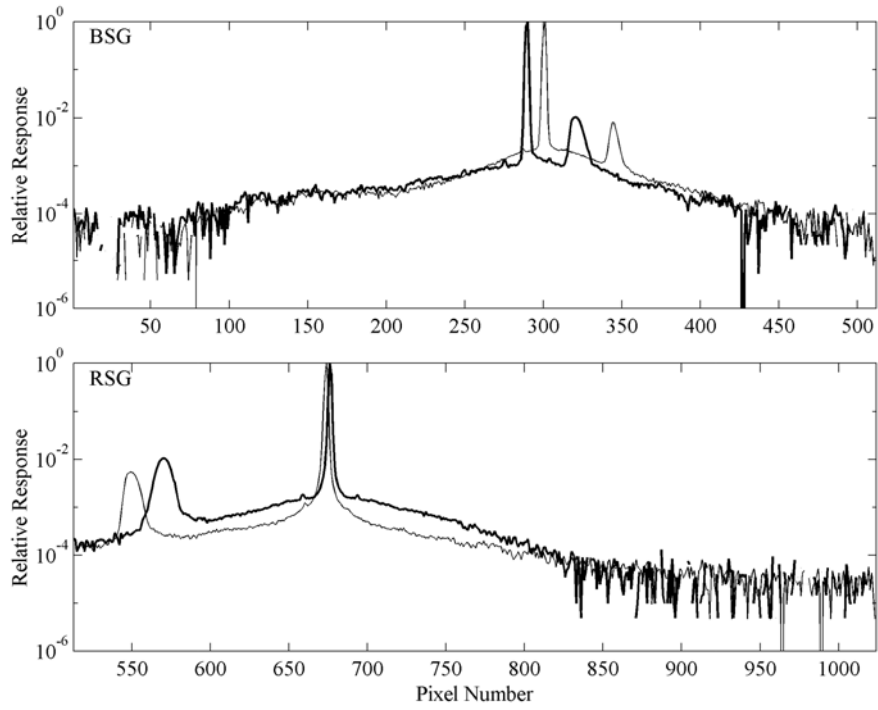
Figure 5.8. Comparison of MOS204/MOBY218 (light solid line) and MOS205/MOBY219 (dark solid line) radiance ports' response to monochromatic excitation.
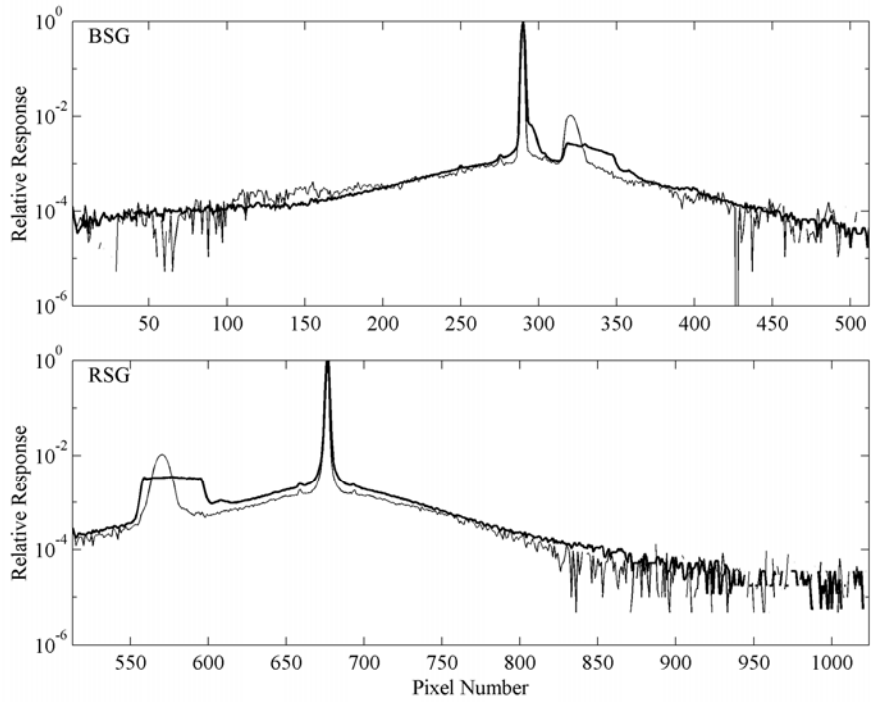

Figure 5.9. Comparison of MOBY radiance arm (light solid line) and MOS (dark solid line) response to monochromatic excitation.
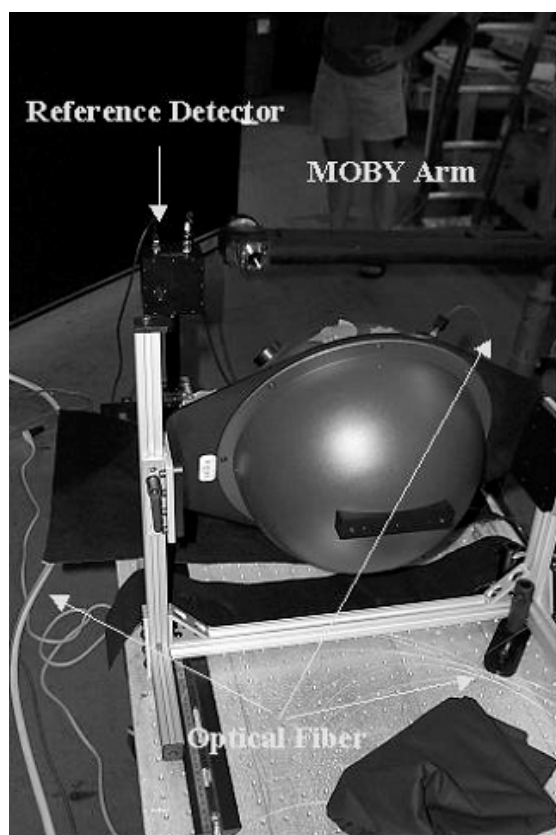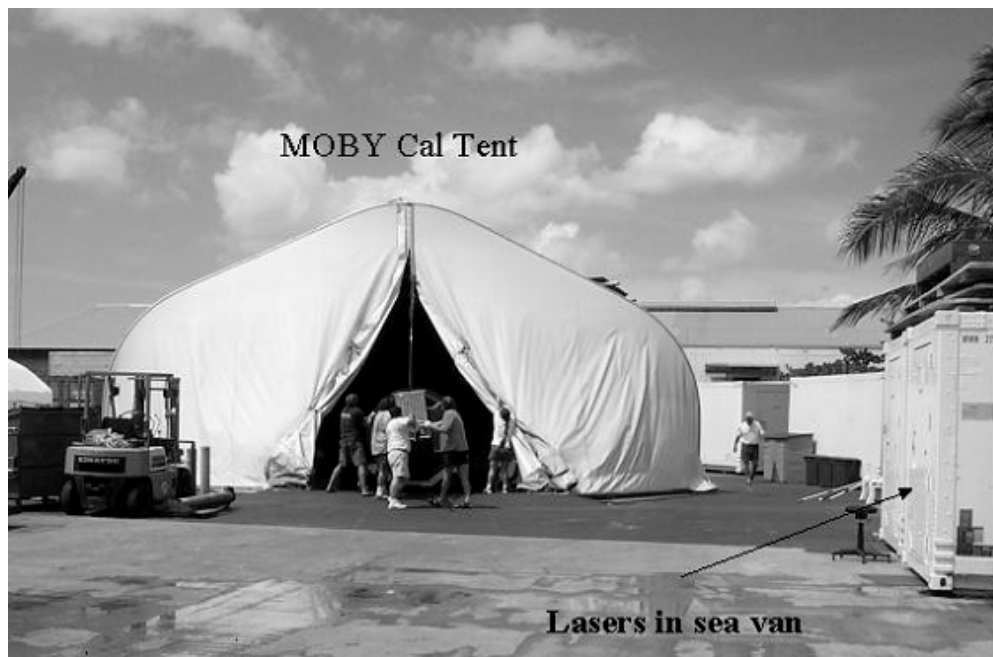
Figure 5.10: Schematic of experimental setup at the MOBY field site at the University of Hawaii Marine Center, Honolulu, Hawaii. (a) Exterior setup showing location of lasers and calibration tent. (b) experimental setup in the calibration tent for measuring the ISS radiance with a collector on the middle MOBY arm.

The output from the lasers was sent into a laser power-controller/stabilizer to reduce power fluctuations in the beam. Portions of the beam were also sent into a wavemeter to determine the wavelength of the laser radiation and into a Fabry-Perot spectrum analyzer so that the mode structure of the laser output could be monitored. The lasers were kept in an air-conditioned sea van and radiation was fiber-coupled into an integrating sphere in the MOBY tent. A portion of the optical fiber was placed in an ultrasonic bath to reduce effects of speckle in the measurement of the output of the ISS. From the sea van, the optical fiber was placed in a garden hose for protection and through an electrical conduit to the MOBY tent. The experimental setup is shown in Fig. 5.10.

The sphere radiance was determined using a calibrated irradiance transfer-standard radiometer. The radiometer is a six-element silicon-transmission trap detector (Eppeldauer and Lynch 2000). It was calibrated for spectral-power responsivity by comparison against a cryogenic radiometer and was equipped with a precision aperture of known area. The sphere radiance is given by the ratio of the measured signal to the trap responsivity times a geometrical flux transfer constant G_D

$$L_{\text{Sphere}} = \frac{S_{\text{Trap}}}{R_{\text{Trap}} * G_D} ,$$

(5.11)

with G_D given by

$$G_D = \left(\frac{A_1 * A_2}{Z^2} \right)\left(1 + \frac{r_1^2 + r_2^2}{Z^4} \right)$$

(5.12)

where we have $Z^2 = r_1^2 + r_2^2 + d^2$, A_1 (r_1) is the sphere exit port area (radius), A_2 (r_2) is the trap aperture area (radius), and d is the distance between the two apertures.

The sphere was equipped with a silicon monitor photodiode. During MOBY measurements, the monitor was calibrated for the sphere radiance over a spectral range of interest using the reference standard trap detector, and then MOBY measurements were made. The monitor signal was recorded for each MOBY measurement.

Communication was established between the laser sea van and the MOBY tent using walkie-talkies or a marine band radio. It was important to properly couple the laser radiation into the optical fiber. During this alignment process, the monitor signal was continuously displayed on a computer in the MOBY tent. Coupling of the laser light into the fiber was adjusted, and the effect on the monitor signal was noted. The laser was properly coupled into the fiber when the monitor signal was maximized. The monitor signal was displayed on a computer screen in the calibration tent. Using commercially available software, the screen was also displayed on a computer in the sea van to simplify the fiber alignment process.

Slit-scatter parameters were determined for the BSG and the RSG coupled to the MOBY arms. To properly model the slit-scatter function (SSF) for the stray-light correction (SLC) algorithm we need the following parameters: (a) the single pixel in-band area; (b) a fit to the OOB slit-scatter function; (c) model for the reflection peaks and (d) model for additional light scatted onto the BSG CCD from radiation in the spectral range from 640 nm to 690 nm. In the following subsections, the basic steps undertaken to derive model parameters for the slit-scatter function are outlined for MOS205/MOBY 219 middle arm L_u port for the BSG and RSG, respectively.

MOS205/MOBY219 BSG in-band area

The stray-light correction terms on the right hand side of Eqs. (5.7) and (5.9) are divided by the normalized in-band area, N. N is given by Eq. 3.3, where the integration is over a 'suitably defined' in-band area

$$N = \int_{ib} \sigma(\lambda_i - \lambda) d\lambda .$$

(5.13)

To determine the in-band area, the laser output was changed in small increments (0.1 nm to 0.2 nm) from 590 nm to 600 nm and an image was acquired at each wavelength. The raw data (ADU/pixel/s) were divided by the sphere radiance, then normalized to a pixel's maximum responsivity. The wavelength of each pixel's maximum responsivity was subtracted, leaving each pixel's normalized responsivity, centered about a relative wavelength of 0 nm, for three adjacent pixels, P420-P422. Fig. 5.11 shows the normalized in-band responsivity of these pixels. Numerically integrating the line shapes gives in-band areas for the three pixels that agree to within 1%. Changing the limits of integration from ± 4 nm to ± 6 nm changed the areas by less than 0.2 %. Fitting to an analytical function also gave results in agreement with the numerical integration. The in-band area and associated relative

standard uncertainty are listed in Table 5.1. In-band scans were repeated over the range from 420 nm to 430 nm to determine the spectral dependence of the bandwidth. No dependence was observed.

Table 5.1. Values and uncertainties in the slit-scatter function derived uncertainties for MOS205/MOBY219 Lu middle arm.

Parameter	Variable	MOS205/MOBY BSG	Uncertainty [%]	MOS205/MOBY RSG	Uncertainty [%]
Normalization	N	0.985	1	1.137	1
Bandwidth	bw	0.5805	0.25	0.8047	0.25
OOB SSF	m_1	0.1142	2	0.164	2
	m_2	113.17	2	90.42	2
	m_3	1.125e-5	25	1.5e-5	25
Reflection Peak Position	l_o	92.485	0.25	343.0125	0.25
	l_1	0.6108	0.25	0.5859	0.25
Reflection Peak Area (P<100)	a_1	0.02599	3	0.0279	3
	a_2	295.0	3	713.997	3
	a_3	33.0	3	25.4843	3
Area (P>100)	b_1	0.02599	3		
	b_2	346.2642	3		
	b_3	13.2884	3		
Off CCD Amplitude	ScaleFactor	0.14	10	NOP	
Reflection Peak Dispersion	c_1	0.6108	0.25	0.5859	0.25

MOS205/MOBY219 BSG out-of-band slit-scatter function component

In modeling the slit-scatter function, we are considering the normalized relative response of the array to monochromatic excitation. To determine the out-of-band (OOB) component of the slit-scatter function, the laser excitation wavelength was fixed at the peak of the response of one of the in-band pixels and a number of images were acquired and averaged. The OOB slit-scatter function is shown in Fig. 5.12. The spectrum, with the center ± 5 pixels masked, was fit to a double exponential of the form

$$y = m_1 \exp\left(-2|x - x_0|\right)/m_2 + m_3 , \qquad (5.14)$$

where x = column number and x_o is the column number with the peak response to the excitation wavelength, and the m_i's are constants determined from the fit. The fit is shown by the solid line in Fig. 5.12, and fit parameters are listed in Table 5.1. Note that there is an apparent 2-pixel shift in the center pixel between the imaged peak (centered at column 419) and the fit peak (x_o = 421). This shift is ignored in the model of the slit-scatter function.

MOS205/MOBY219 BSG Reflection peaks

The amount of light scattered onto the CCD in this reflection peak is significant. It is therefore necessary to include a model for these peaks in the general model for the slit-scatter function. For the model, we want to know what fraction of the incident light imaged onto some pixel is measured by the pixel under consideration. The modeling is complicated by the fact that the reflection peak area is a strong function of position and the rate at which it moves across the CCD with changing wavelength differs from the primary image.

To model the incident light scattered onto a particular pixel, we first need the relationship between the reflection peak position and the excitation peak position. This relationship, shown in Fig. 5.13, was fit to a linear regression, given by the solid line in the figure. Values are given in Table 5.1.

To calculate the fraction of the incident light that is in the reflection peak, we want to compare the integrated areas of the reflection peaks to the areas of the fundamental peak. The primary peaks in the data set are first

normalized to 1. The relative reflection peak data, plotted as a function of separation from the primary image (in pixels), are shown in Fig. 5.14. There is a large variance in both the amplitude and the total area under each reflection peak, but we need to consider that not all excitation wavelengths were centered on a pixel's response, so the reflection peaks may not be properly normalized to a pixel's peak response. Consequently, it was necessary to correct the amplitude of the reflection peaks in Fig. 5.14 for the excitation offset.

The in-band data set was fit to a Gaussian distribution given by

$$y = p_o + p_1 \exp\left(-\frac{1}{2}\left(\frac{x-p_2}{p_3} \right)^2 \right), \tag{5.15}$$

where the p_i's are constants determined from the fit.

We get a reasonable fit, shown in Fig. 5.15, though the area is slightly underestimated because the fit does not represent the right-hand shoulder well. The calculated area from the Gaussian fit agrees with the numerically integrated value to within 1 %. In Eq. (5.15), p_1 is the amplitude; p_2 is the center or offset; and p_3 is the width. To correct the excitation peak, we fit the primary image for the reflection peak data set to a Gaussian lineshape with a fixed width determined by the in-band fit. Note that to obtain the proper width for the fitting routine, it is necessary to convert the width from wavelength to pixel by dividing the width (nm) determined by the fit in Fig. 5.15 by the pixel-to-pixel spacing of the BSG (0.58 nm/pixel).

With the width fixed, we are only concerned with the amplitude determination (or the value of p_1) in Eq. 3.4. Each primary image peak was fit to Eq. (5.15), and results are summarized in Table 5.1. Corrections as large as 26 % are applied to the reflectance peak amplitude data set. Note that there is often a small shift in the peak position as well. The shift is less than 0.5 pixels and is not included in the modeled reflection peak position.

The corrected, normalized reflection peak data set is shown in Fig. 5.16. The 440 nm data set had an additional correction applied to make the haze component similar to the other data sets. One possible explanation for the apparent increase in scattered light is a wavelength-instability problem with the 440 nm diode laser used to acquire the spectrum. This would broaden the primary image and lead to an overestimation of the reflection peak amplitude in the modeled slit-scatter function.

For the slit-scatter function model, we are interested in the fraction of the in-band radiation scattered into the reflection peak. The amplitude-corrected reflection peaks are fit to Gaussian line shapes, giving the reflection peak area as a function of excitation wavelength or peak pixel. The reflection peak area as a function of position is shown in Fig. 5.17. The solid line is the fit to the data using Eq. (5.16) for pixels greater than 100 and Eq. (5.17) for pixels less than 100; *i.e.*

$$y = a_1 \big/ (1 + (x/a_2)^{a_3}) \text{ , and} \tag{5.16}$$

$$y = b_1 \big/ (1 + ((350-x)/b_2)^{b_3}) \text{ .} \tag{5.17}$$

where x refers to the pixel under consideration.

The area must be further corrected for the increased rate at which the reflection peak moves through a particular pixel compared with the primary image. The primary image moves at a rate of approximately 0.58 nm/pixel while the reflection peak's dispersion is 0.35 nm/pixel. This will be discussed further, in subsections to follow, with regard to the red spectrograph.
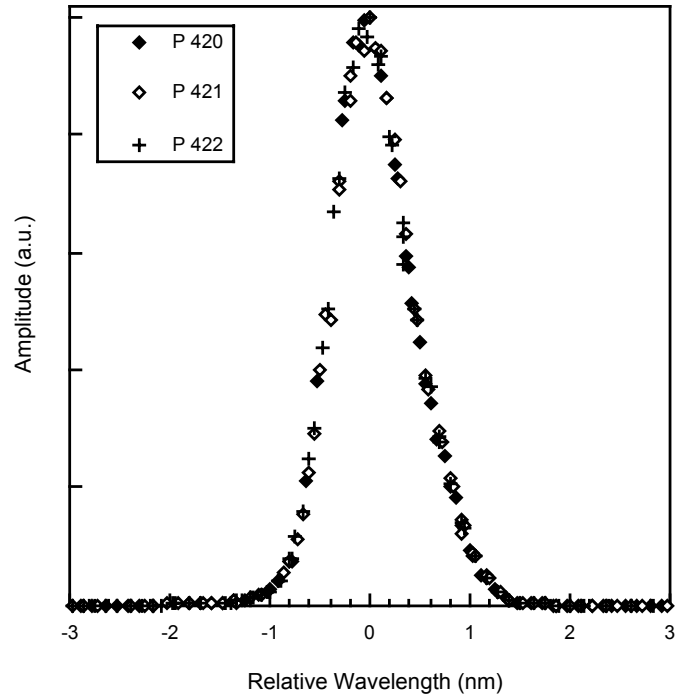
Figure 5.11: Normalized, center-wavelength-subtracted responsivity of BSG pixels 420, 421 and 422.
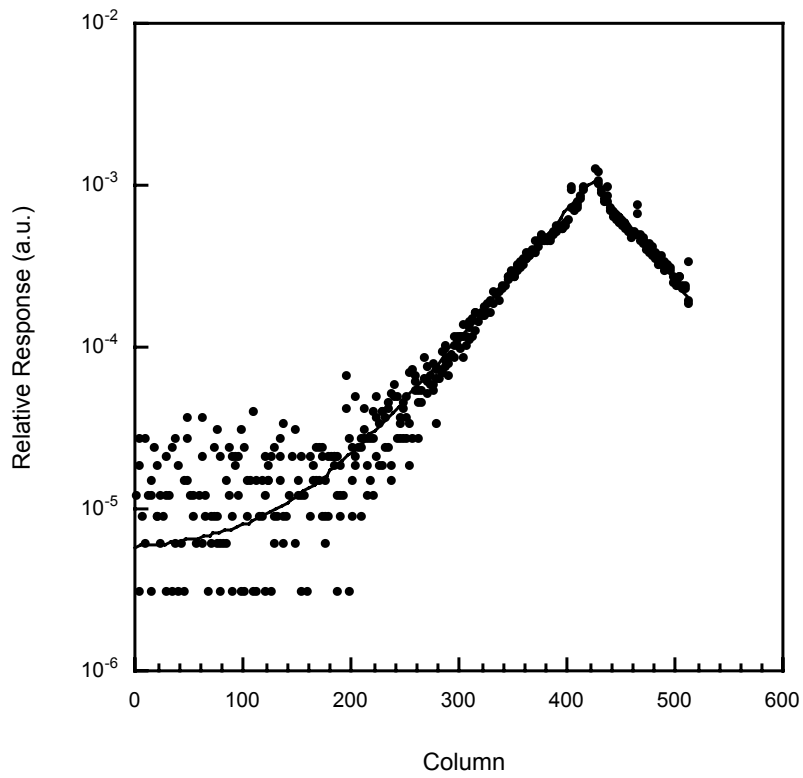

Figure 5.12: MOS205 BSG out-of-band slit-scatter function.
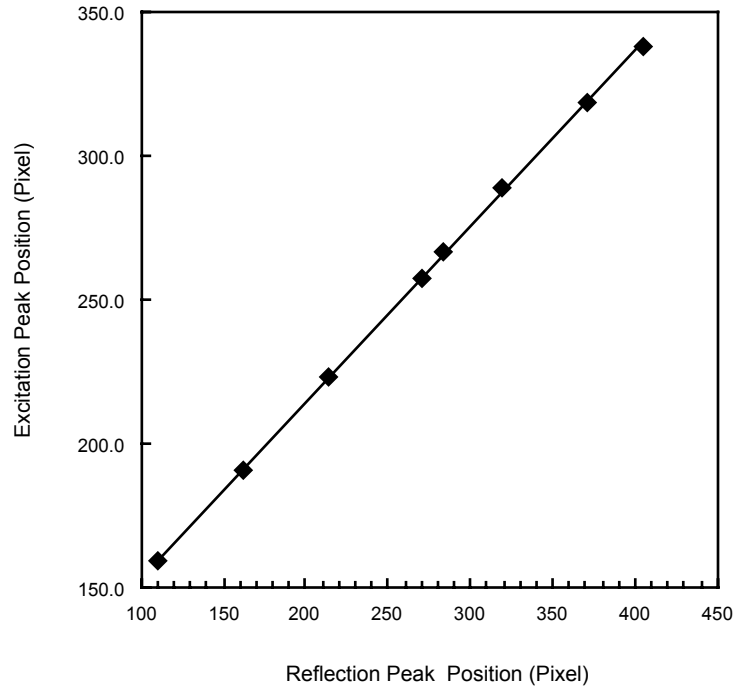
Figure 5.13: Location of the MOS205 BSG primary image versus the position of the reflection peak, with the solid line a fit to the data.
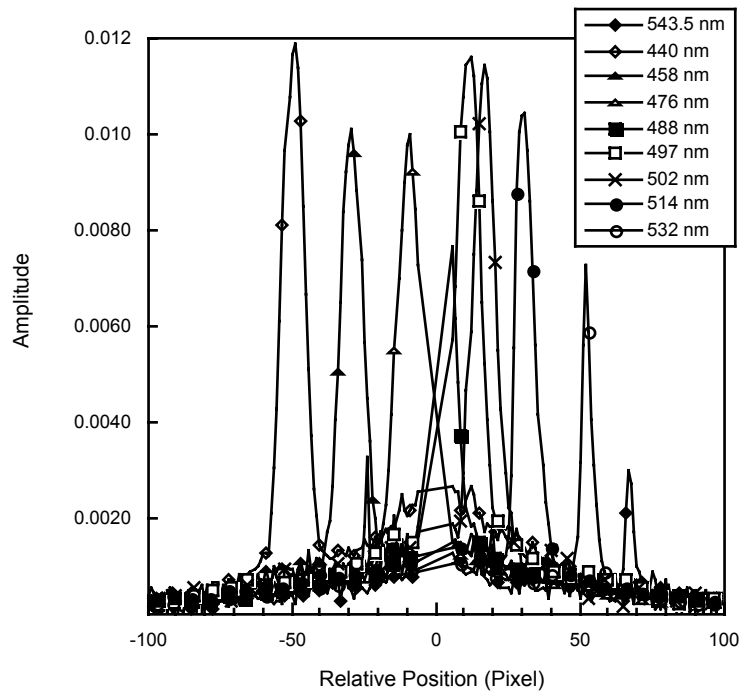

Figure 5.14: MOS205/MOBY219 L_uMid BSG reflection peak data set, uncorrected for the amplitude of the excitation peak
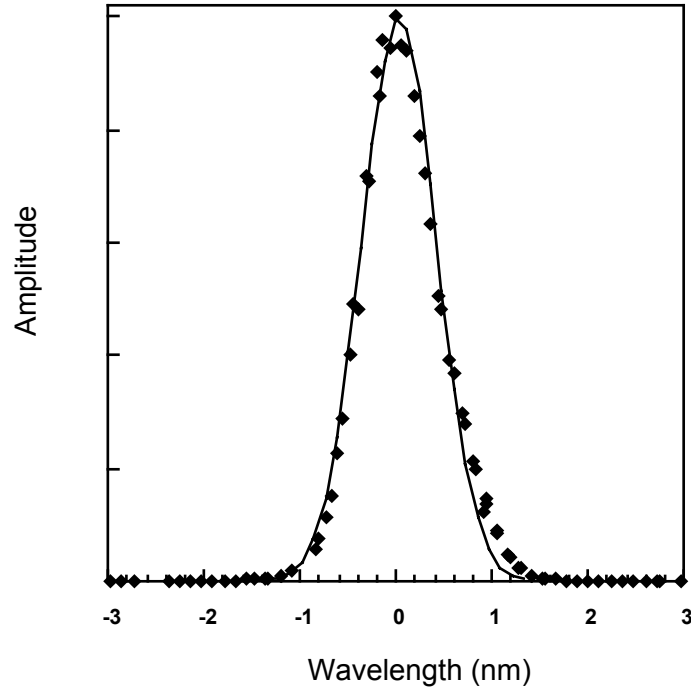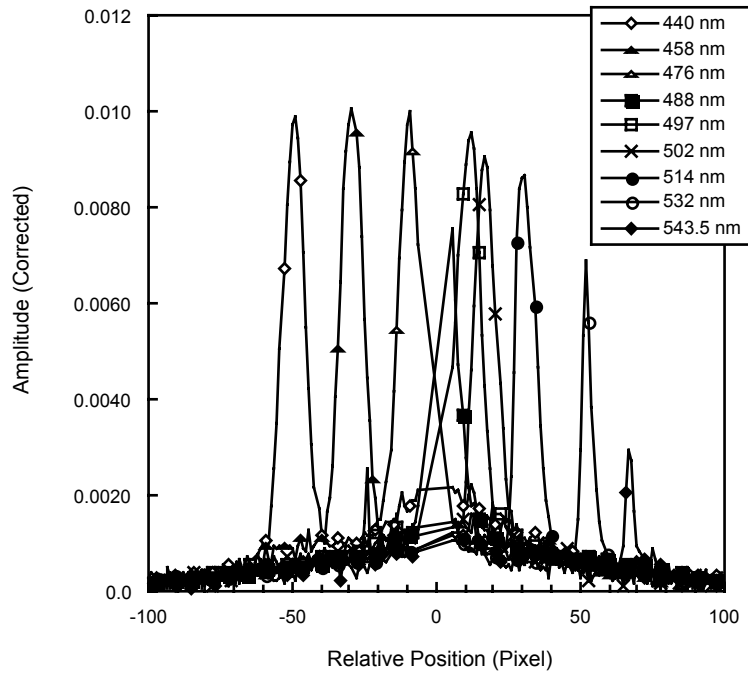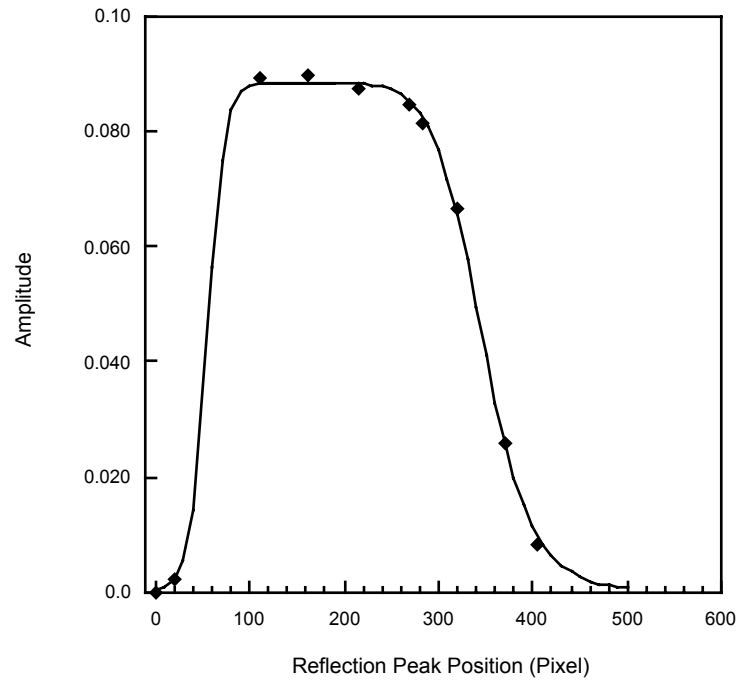
Figure 5.15: Gaussian fit to the MOS205/MOBY219 BSG in-band data set.

Figure 5.16: MOS205/MOBY219 LuMid BSG reflection peak data set, corrected for the amplitude of the excitation peak.

Figure 5.17: Reflection peak area as a function of position; the solid line is a fit to the data.
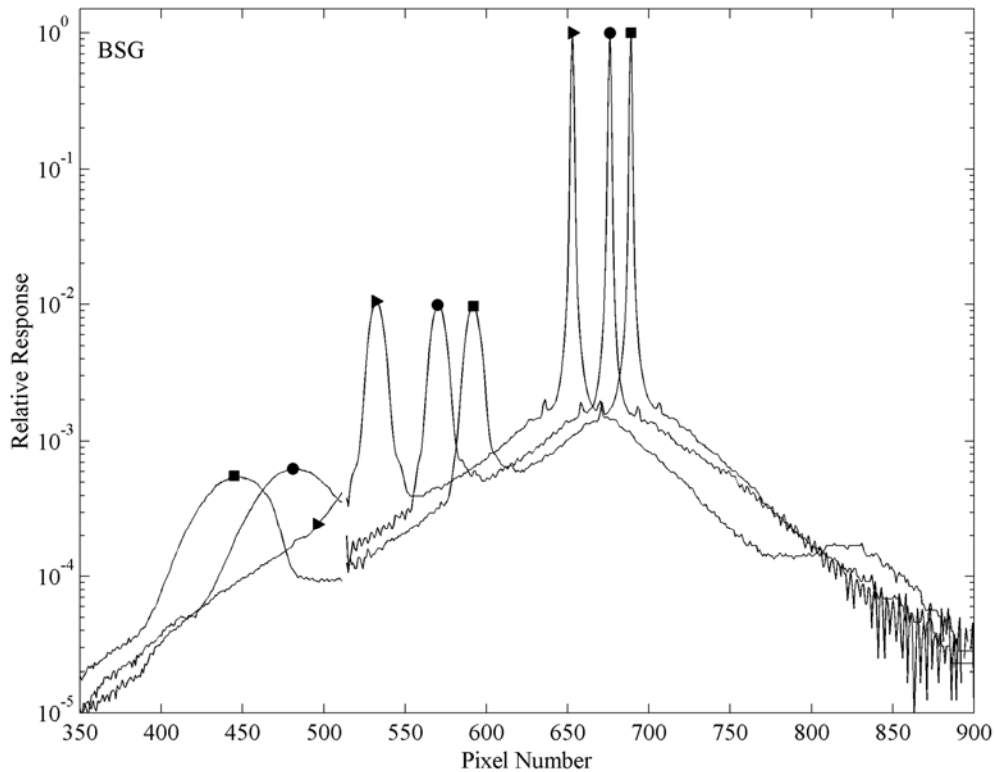
Figure 5.18: Response of BSG pixels 400 to 511 and full RSG response for discrete laser excitation in the range from 640 nm to 690 nm.

M205/MOBY219 BSG Off-CCD Scattering

There is additional scattering onto the right edge of the CCD from light not directly imaged onto it. In Fig. 5.18, we show the responsivity of pixels 400 to 511 for the BSG from discrete laser excitation in the range from 640 nm to 690 nm. Tunable lasers in the 640 nm to 690 nm spectral range were not available during the field measurements and we do not have enough spectral data to directly model BSG stray light effects in this range. Consequently, the magnitude of this contribution was empirically fit to validation source data sets (discussed in Section 5) by including a quadratic term in the BSG slit-scatter function in the overlap region (pixels 400 to 511).

MOS205/MOBY219 Red Spectrograph (RSG)

The same set of model slit-scatter parameters was determined for the MOS205/MOBY219 RSG, with the exception of the off CCD term. Flux transmitted through the dichroic beamsplitter, incident on the RSG, falls off rapidly below 600 nm. Essentially no light below 550 nm is incident on the CCD, so a term to account for off-CCD scattering is not included in the RSG model slit-scatter function.

MOS205/M219RSG in-band area

Images were acquired as the excitation wavelength was tuned in small steps over the spectral range from 740 nm to 750 nm. The in-band areas of three adjacent pixels P756, P757, and P758, shown in Fig. 5.19, were determined. The areas agreed to within 0.25 %; changing the limits of integration from ± 4 nm to ± 6 nm changed the in-band area less than 0.2 %. The in-band area and uncertainty are listed in Table 5.1.

MOS205/M219 LuMid RSG OOB Slit-scatter Function

The peak-normalized OOB slit-scatter function, along with the double-exponential fit to the data [Eq. (5.13)] are shown in Fig. 5.20. Note that the reflection peak was masked for this fit as well as the in-band ± 5 center pixels. There is a 0.6 pixel offset from center between the image and the fit. This small offset is ignored in the model. Parameters are listed in Table 5.1.

MOS205/M219 LuMid RSG Reflection peaks

Images were acquired for excitation wavelengths ranging from 640 nm to 800 nm. A linear fit to the relationship between the reflection peak and the excitation peak positions is shown by the solid line in Fig. 5.21. Next the central peaks were fit to a Gaussian lineshape, with a width determined from the in-band scan. As with the BSG, these data are used to properly normalize the reflection peak amplitude. For the RSG, the dispersion is 0.804 nm/pixel. Uncorrected and corrected reflection peak data sets are shown in Figs. 5.22 and 5.23. Note that there is an apparent increase in the amplitude of the reflection peak for the first 3 wavelengths, where diode lasers were used for excitation. As with the BSG 440 nm data set, it may be a consequence of the multi-mode spectral output of the diode lasers used for this spectral region.

The amplitude-corrected reflection peaks are fit to Gaussian functions with a linear offset, giving the reflection peak area as a function of excitation peak pixel. The areas are again corrected for the rate at which the reflection peak moves through a particular pixel. For example, consider the RSG fine scans around 740 nm. In this spectral region, a reflectance peak is observed around 700 nm (pixel 702), as shown in Fig. 5.24. As the excitation is scanned in small steps, the response of pixel 702 can be measured and compared with the spectral width of the reflection peak in Fig. 5.24. Fig. 5.25(a) shows the reflection peak observed for 740.3 nm excitation, while Fig. 5.25(b) shows the spectral response of pixel P702. Both are plotted in wavelength scale using a dispersion of 0.804 nm/pixel for Fig. 5.25(a). Note the reduction in the width of the P702 reflection peak with respect to the reflection peak image from monochromatic excitation. This apparent reduction occurs because of the difference in the spectral dispersion of the primary and reflection peak images, and must be taken into account in the model of the reflection peak amplitude.

The final results are graphically illustrated in Fig. 5.26 with the fit to Eq. (5.16) shown by the solid line. Fit parameters are listed in Table 5.1.
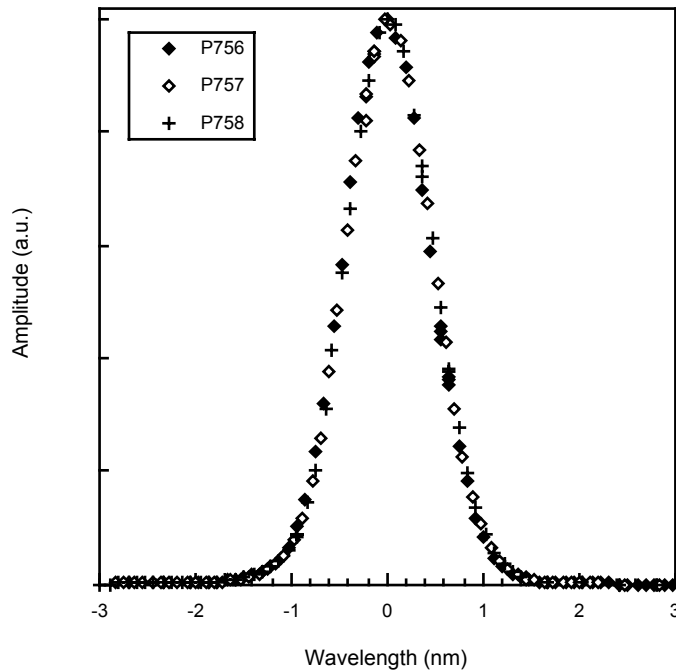
Figure 5.19: Center-wavelength subtracted, peak normalized, MOS205/MOBY219 RSG in-band scans for pixels 756,757, and 758.
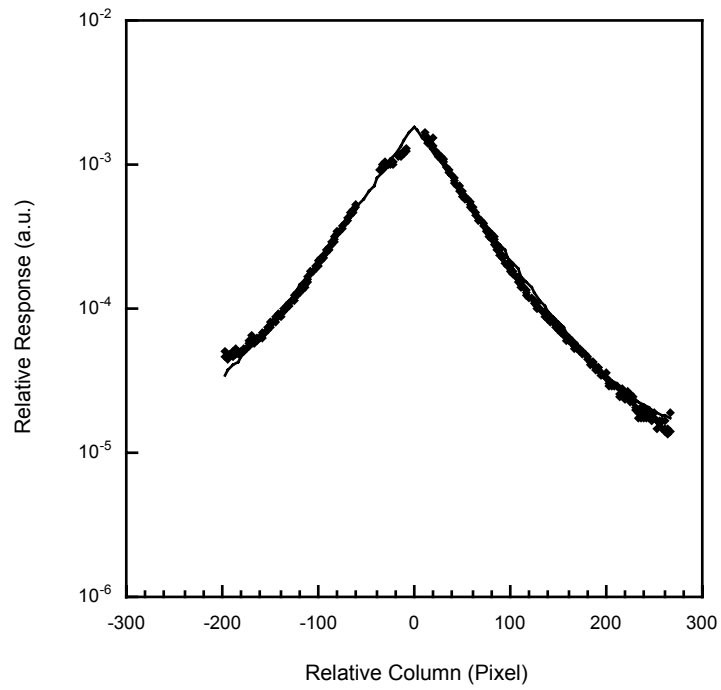

Figure 5.20: Peak normalized MOS205/MOBY219 RSG out-of-band slit-scatter function.
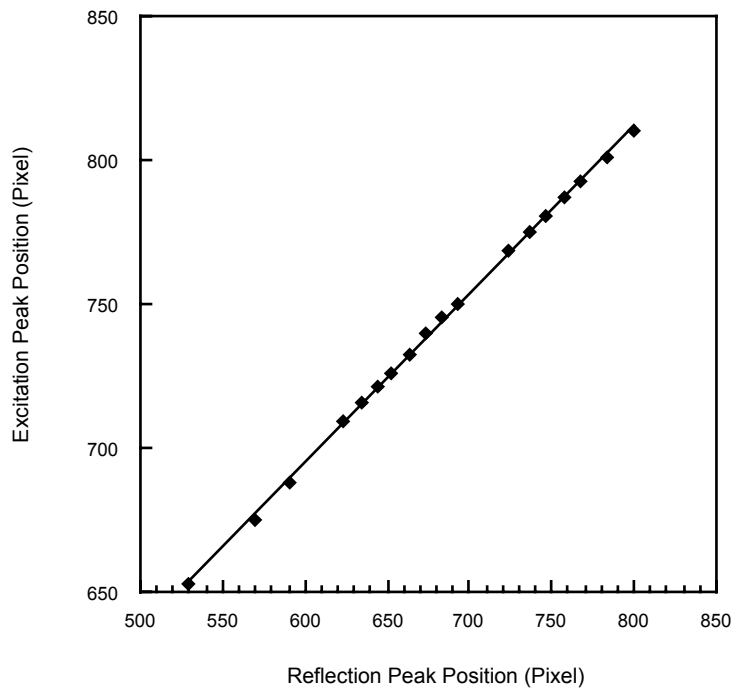

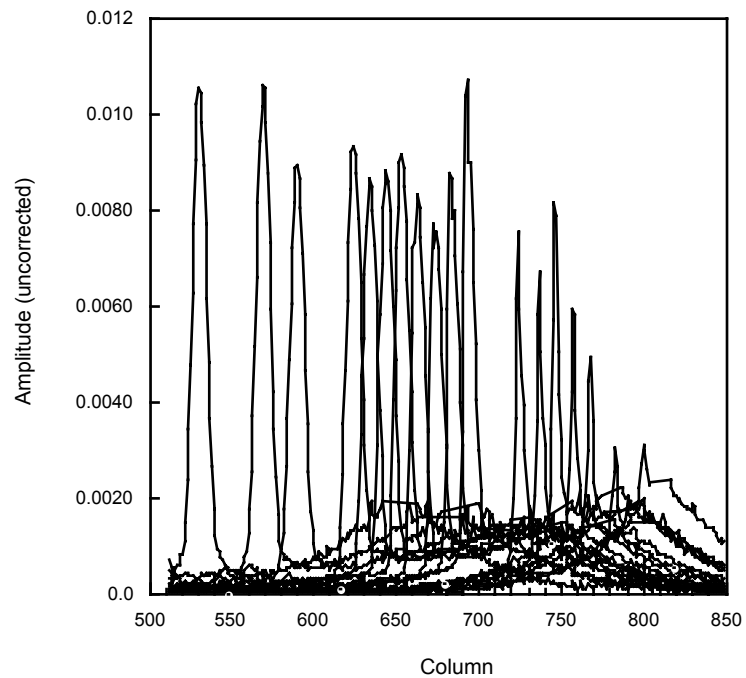Figure 5.21: MOS205/MOBY219 excitation peak position as a function of reflection peak position.

Figure 5.22: MOS205/MOBY219 uncorrected reflection peak data set.
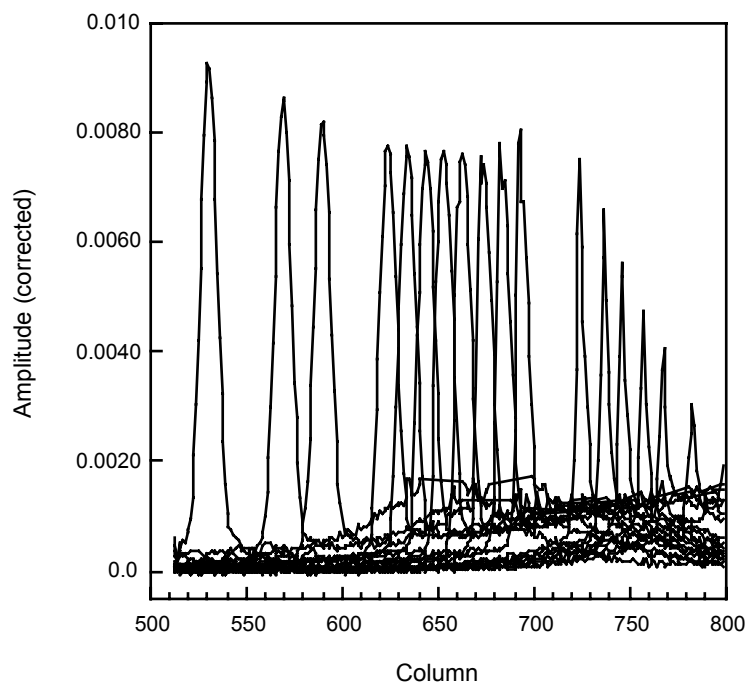

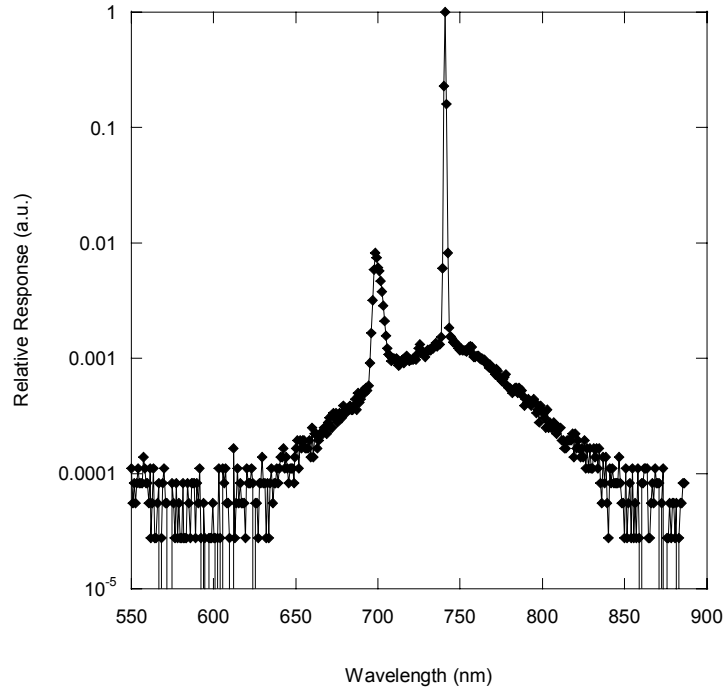Figure 5.23: MOS205/MOBY219 corrected reflection peak data set.

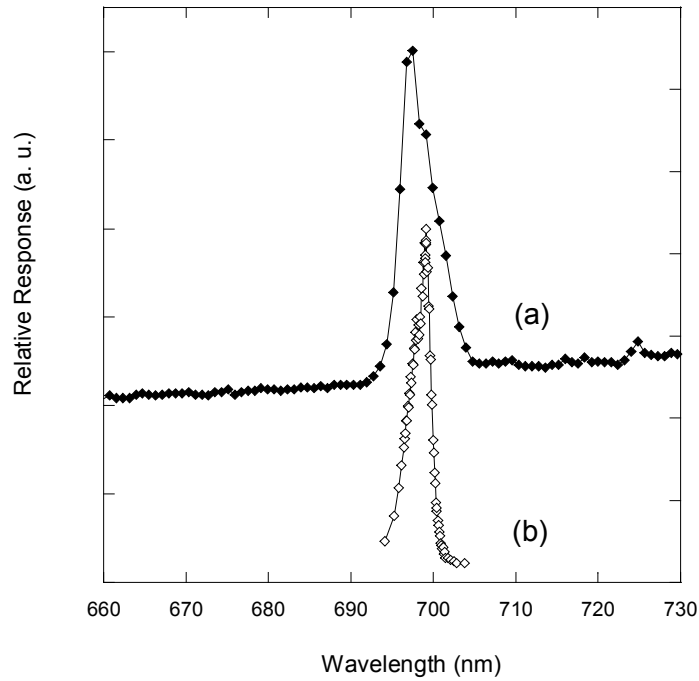Figure 5.24: Relative RSG response to monochromatic excitation at 740.3 nm.

Figure 5.25: (a) Reflection peak for RSG response to monochromatic excitation at 740.3 nm. (b) Response of pixel 702 as the excitation wavelength is changed from 695 nm to 705 nm.
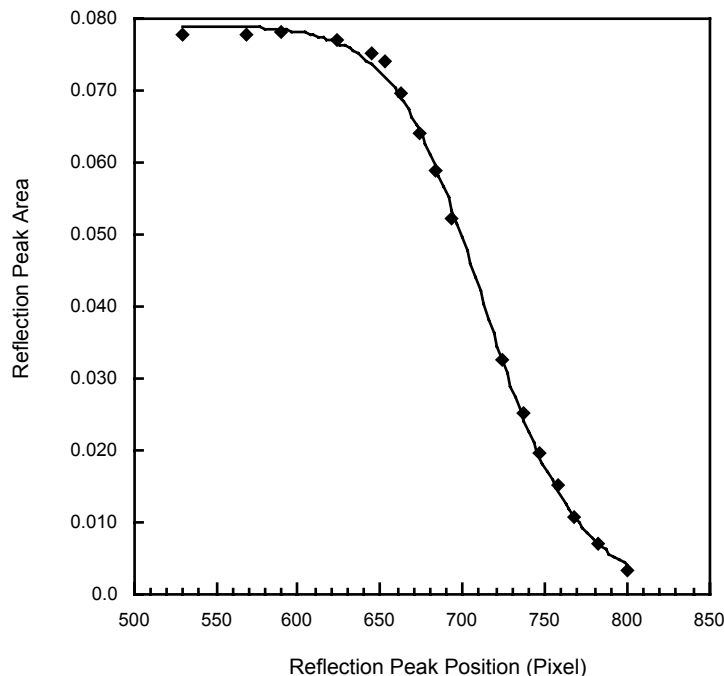
Figure 5.26: MOS205/MOBY219 reflection peak amplitude as a function of reflection peak position.

5.4 STRAY-LIGHT CORRECTION OF MOBY

The parameters developed in Section 5.3 for MOS205/MOBY219 were incorporated into the stray-light correction algorithm described in Section 5.2. The algorithm was used to correct MOBY calibration and in-water data sets. MOBY was calibrated using a lamp-illuminated integrating sphere calibrated for spectral radiance. The iterative stray-light correction procedure described in Section 5.2 [Eq. (5.7)] was applied to the measured signal. Iterations were repeated until a stable solution was reached; a solution that changed by less than 0.1 % from the previous iteration was considered stable. Typically, a stable solution was reached after 4 to 5 iterations. The uncorrected responsivity and the stray-light corrected responsivities are shown in Fig. 5.27. In Fig. 5.28, the ratio of the corrected responsivity to the uncorrected responsivity is shown. Stray-light is responsible for approximately 10 % of the signal over much of the spectral range, increasing rapidly below 400 nm for the BSG, and below 640 nm for the RSG. The rectangular increase in the corrected over uncorrected ratio (reduction in stray-light) for the BSG near 500 nm occurs in the region where the reflection peak coincides with the primary image.

Using the stray-light-corrected responsivities, MOBY up-welling radiance data are corrected using Eq. (5.9). Uncorrected and corrected radiance measured by each arm is shown in Fig. 5.29, and the ratio of uncorrected to corrected up-welling radiance in Fig. 5.30. Note the dramatic improvement in the agreement between the two spectrographs in their overlap region in the stray-light-corrected results. There is also a significant increase in the measured up-welling radiance below 400 nm.

MOBY is used to vicariously calibrate SeaWiFS by providing measurements of water-leaving radiance. The water-leaving radiance is determined from the up-welling radiance according to Clark (Clark *et al*. 2002a; Clark *et al*. 2002b). The water-leaving radiance was calculated for stray-light-corrected and uncorrected data sets. The correction factor — or ratio of corrected to uncorrected water-leaving radiance — is shown in Fig. 5.31. We again see a strong increase in the corrected water-leaving radiance below 400 nm, reaching a value of approximately 40 % for 360 nm radiation. The corrected water-leaving radiance is less than the uncorrected values for wavelengths longer than 500 nm. The decrease rises to approximately 20 % for the BSG beyond 600 nm.

Band-integrated stray-light-correction factors for water-leaving radiance for the SeaWiFS bands are listed in Table 5.2. The correction factors range from +8.5 % for Band 1 to –2.5 % for Band 4.

Table 5.2. Band-integrated stray-light-correction factors for
water-leaving radiance in the SeaWiFS bands.

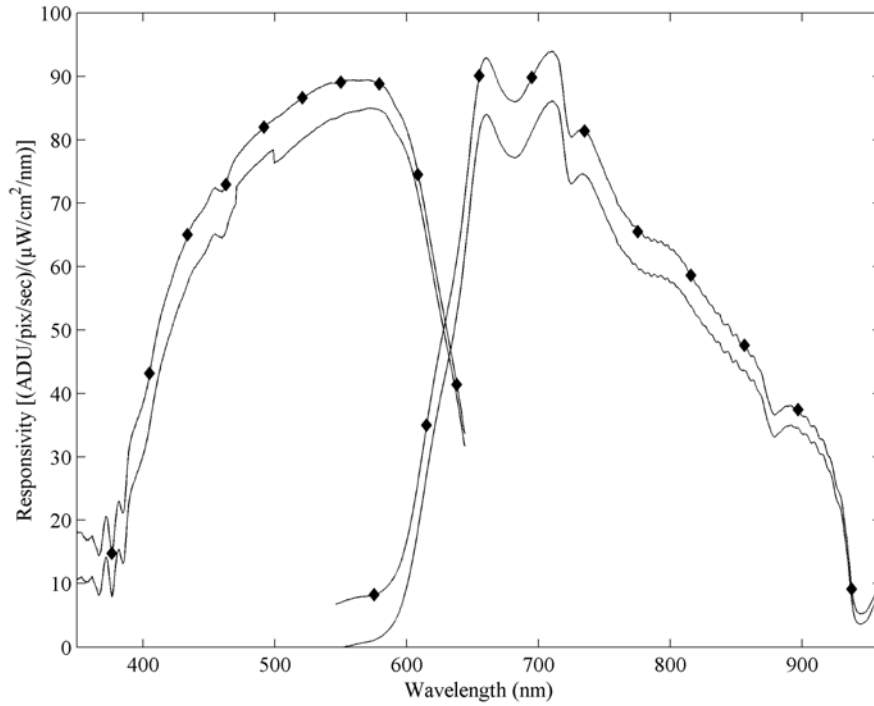| SeaWiFS Band	Ratio Corrected/Uncorrected L_w
1	1.085
2	1.033
3	1.012
4	0.976
5	0.979
6	1.014

Figure 5.27: Uncorrected (diamonds) and stray-light-corrected (solid line) responsivity of MOS205/MOBY219 radiance arms.
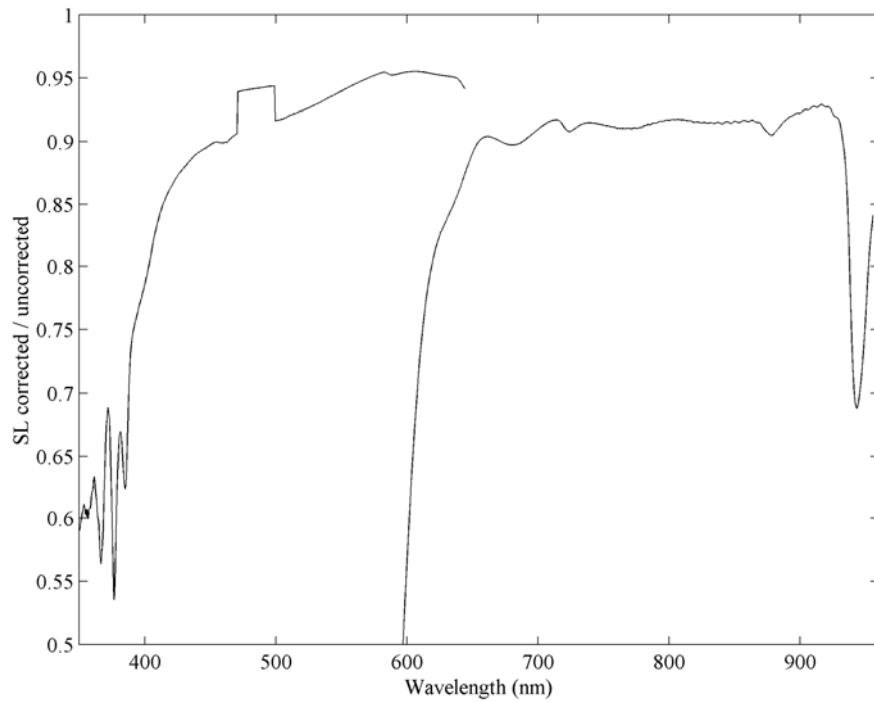

Figure 5.28: Ratio of the MOS205/MOBY219 L_uMid radiance arm corrected responsivity to the uncorrected responsivity.
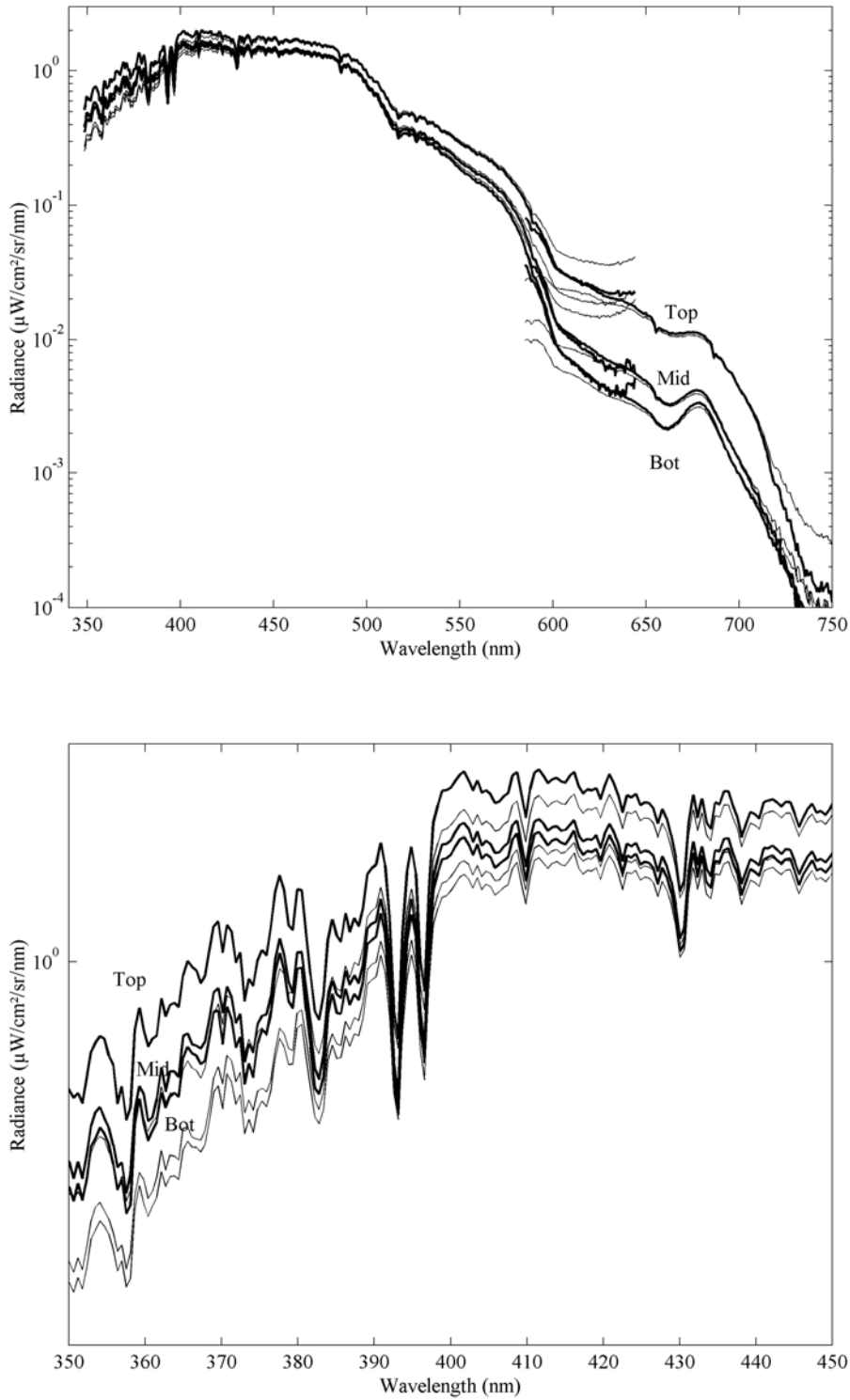
Figure 5.29: Uncorrected (thin solid line) and corrected (thick solid line) up-welling radiance measured by each MOS205/MOBY219 arm. (Bottom panel) Expanded view in the UV region.
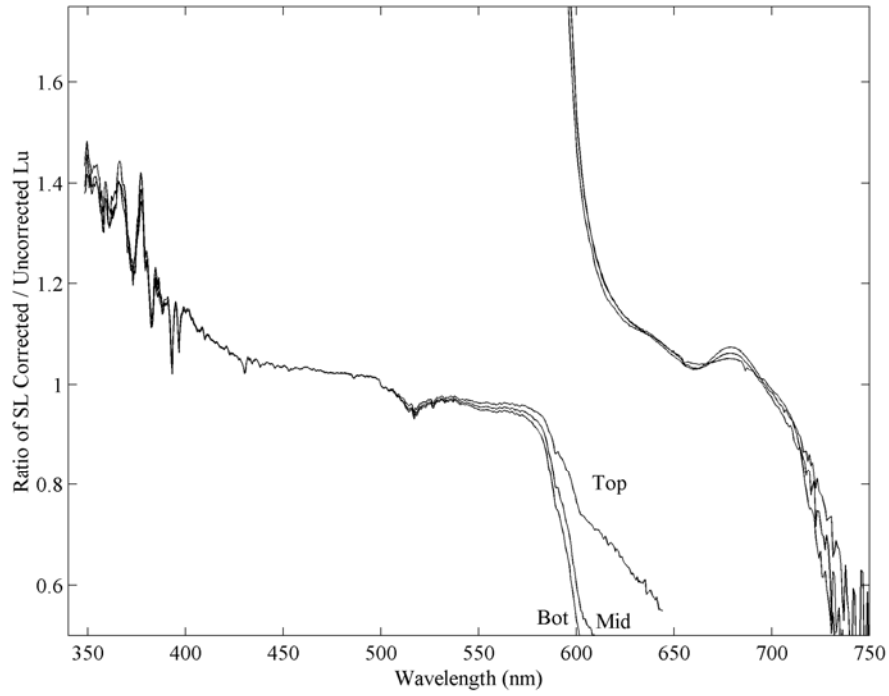
Figure 5.30: Ratio of corrected to uncorrected up-welling radiance L_u measured by each MOS205/MOBY219 arm.
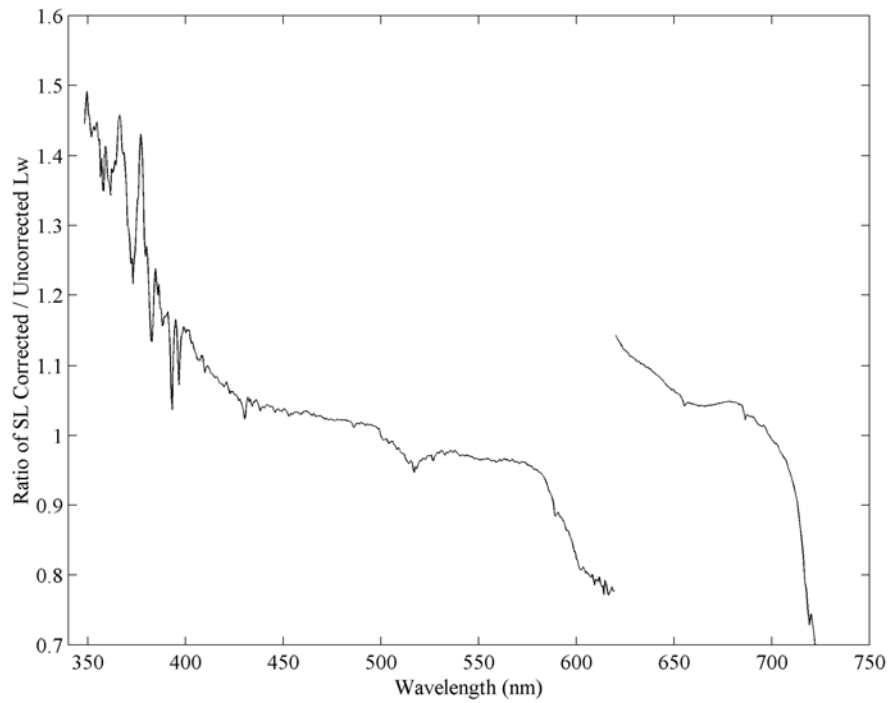

Figure 5.31: Ratio of stray-light-corrected to uncorrected water-leaving radiance L_W measured by MOS205/MOBY219.

5.5 ALGORITHM VALIDATION

To validate the stray-light correction model, a Colored Source (CS) was developed. Different relative spectral distributions were realized using glass and interference filters and a lamp-illuminated integrating sphere source. The spectral radiance for the CS configurations was determined separately using a calibrated spectroradiometer. The SLC algorithm was validated by comparing the corrected spectral radiances from measurements with MOBY to the known CS spectral radiances.

A lamp-illuminated integrating sphere source, model OL420 from Optronic Laboratories,[10] was used for the CS. Briefly, it is a 20.32 cm diameter, externally illuminated sphere that is coated with barium sulfate. The exit aperture is 5.72 cm in diameter and the entrance aperture is orientated 90° with respect to the exit aperture. Quartz windows on both apertures protect the sphere from contamination. A monitor detector, fitted with a photopic filter, is mounted in the wall of the sphere and its output voltage is recorded during operation.
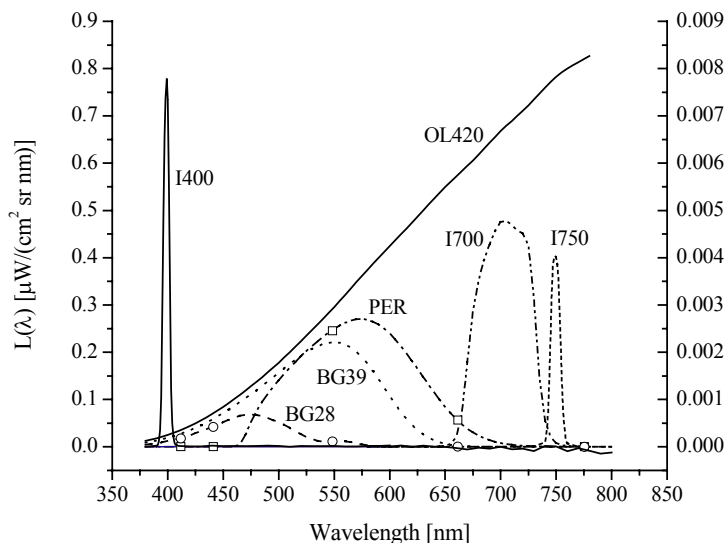

Figure 5.32: Spectral radiance of the OL420 Colored Source with different filters. The radiance of the CS with the I400 nm interference filter, which is a very low level, is shown on the right-hand axis. VXR measurements of the CS are given by the open symbols.

For the CS, we utilized the filter slide that is located between the lamp and the entrance aperture. Six CS configurations were possible, with each filter in a corresponding filter slide for ease of use and minimization of contamination through handling. Three colored glass filters were used: Schott BG28 and BG39[11], and CVI[12] PER filter, producing blue, turquoise and photopic (green) spectral distributions. Three interference filters were used, centered at 400 nm, 700 nm, and 750 nm, with full-width half-maximum (FWHM) bandwidths of 10 nm, 45 nm and 10 nm, respectively.

---

[10] Certain commercial equipment, instruments, or materials are identified in this paper to foster understanding. Such identification does not imply recommendation or endorsement by the National Institute of Standards and Technology, nor does it imply that the materials or equipment identified are necessarily the best available for the purpose.

[11] Schott Glass Corporation (www.us.schott.com).

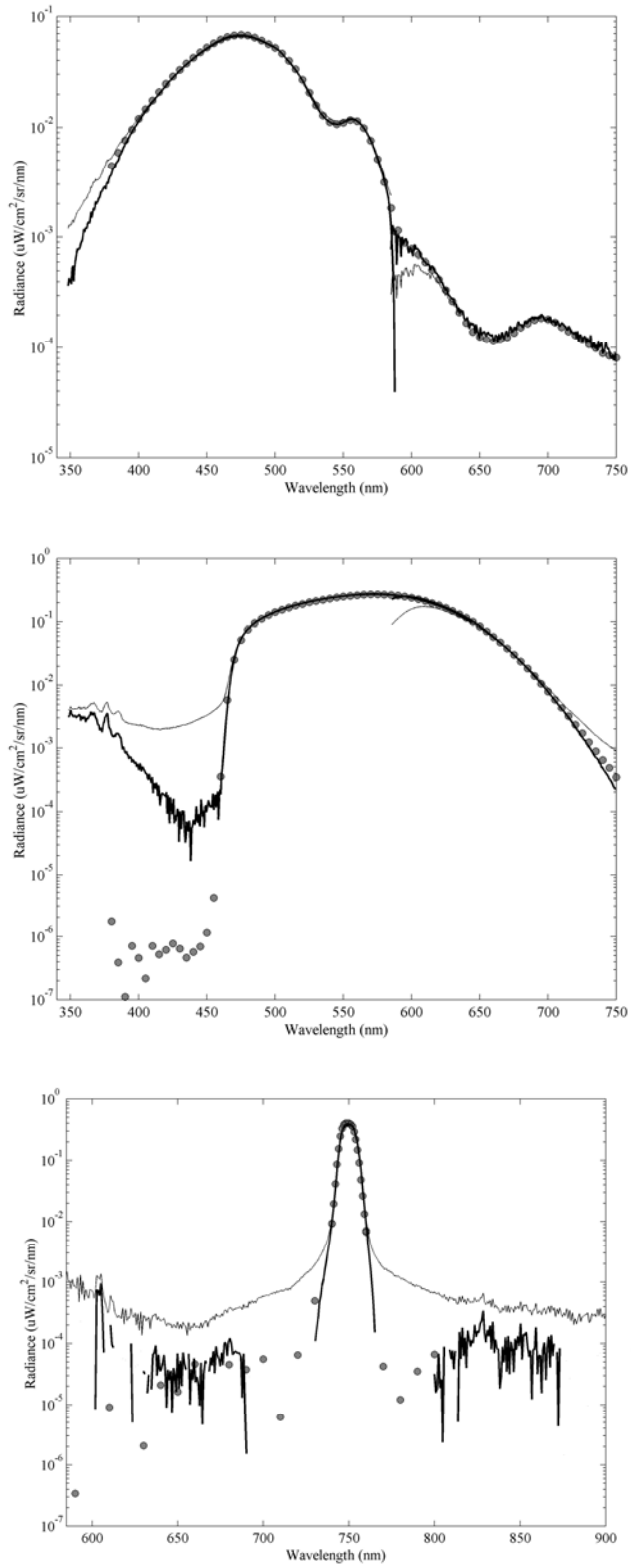[12] CVI Laser Corporation, Albuquerque, NM.

Figure 5.33: Uncorrected (thin line) and stray-light-corrected (dark line) and 'true' (gray circles) measured radiance of the Colored Source with (a) BG28, (b) PER, and (c) I750 filters.

The OL420 was calibrated for spectral radiance on the NIST Facility for Spectroradiometric Calibrations (FASCAL) (Walker *et al*. 1987) in March 2001. The spectral radiances for the PER, BG28, and BG39 configurations of the CS were determined at NIST in May 2001 using a reference spectroradiometer. The instrument is a double-grating, scanning monochromator (Brown and Ohno 1999). It has been fully characterized, with a stray-light factor of less than 10^{-6}. For the CS calibration, the bandpass was set to 5 nm FWHM and a wavelength step of 5 nm was used. For determinations of the CS spectral radiances, the unfiltered OL420 was used to calibrate the scanning monochromator. Typical spectral radiances for the six configurations are shown in Fig. 5.32. The reference spectroradiometer is not a field instrument, and was not transported to the MOBY field site.

During the field deployments, the EOS/NIST Visible Transfer Radiometer (VXR) was used to verify the CS spectral radiances. The VXR is a six-channel filter radiometer (Butler *et al*. 1999), and comparison to the reference spectroradiometer results could only be done where the VXR filter channels coincided with measurable output for the CS configurations. The agreement with the PER was -0.8 % at 548 nm and +1.9 % at 661 nm; with the BG28, it was -3 % at 441 nm and -0.7 % at 548 nm, where negative values indicate the VXR values were lower than the reference spectroradiometer. The VXR results are shown as symbols in Fig. 5.32.

The CS was measured by the radiance ports on the upper or middle buoy arms. The results for the source BG28, PER, and I750 filters are shown in Fig. 5.33. The spectral radiances derived using MOBY are shown with and without correction for stray light along with the spectral radiances for the CS configurations determined using the reference spectroradiometer. Within the in-band spectral regions, the corrected MOBY values agree with the CS spectral radiances to within 5 %.

The out-of-band regions are an important test of the stray-light-correction algorithm. The BG28 configuration decreases by an order of magnitude in the crossover region between the BSG and the RSG, similar to the behavior seen in MOBY waters [see Fig. 5.33(a)]. For this configuration, the correction algorithm was sensitive to the parameters for the off-CCD scattering, resulting in under- or over-correction in the overlap region. We determined the off-CCD parameters by minimizing the differences between the two spectrographs for the BG28 configuration.

Figure 5.33(a) shows that MOBY overestimates the spectral radiance as the wavelength decreases if not corrected for effects arising from stray light. The PER configuration, shown in Fig. 5.33(b), is an excellent test of the ability of the SLC algorithm for the shorter measurement wavelengths in the BSG. The spectral radiance in the region below 450 nm for the PER configuration decreases by more than 10^{-6} compared to the maximum value. Uncorrected, the MOBY values are discrepant by more than three decades in this spectral region. With correction for stray light, the agreement is improved substantially.

The inability to correct at the shortest wavelengths, below 400 nm, is understood in terms of the low system responsivity in this spectral region.

A test of the algorithm for the RSG is shown in Fig. 5.33(c) using the I750 interference filter (peak transmittance at 750 nm). In the out-of-band region, the uncorrected MOBY values are discrepant by a factor of 10 to 100, but the corrected values are in good agreement.

5.6 UNCERTAINTIES

A Monte Carlo approach was used to estimate the uncertainties in the stray-light-correction factors for MOBY up-welling and water-leaving radiance measurements. Model slit-scatter function parameters were input into the stray-light correction algorithm using mean values given in Table 5.1 and a random normal distribution with uncertainties given in Table 5.3. Uncertainties are approximately a factor of 2 larger than those given in Table 5.1 to account for possible additional uncertainties in the model parameters arising from changing environmental conditions and other unknown factors. The full stray-light correction algorithm - correcting both the responsivity and the in-water data - was run 100 times for a typical in-water spectrum and mean correction factors and uncertainties calculated. Typical results for the BSG are shown in Fig. 5.34 for MOS205/MOBY219 LuTop. Both the correction factor and the associated relative uncertainty is less than 1 % over the spectral range from 420 nm to 590 nm and both increase rapidly below 400 nm and above 600 nm, rising to approximately 8 % at the ends of the array: 360 nm and 640 nm, respectively.

   Similarly, the uncertainty in the stray-light-correction factor for derived water-leaving radiance was determined, as shown in Fig. 5.35. The uncertainty in Lw is larger than the uncertainty in Lu, with a 14 % uncertainty in the stray-light-correction factor at 360 nm. In Table 5.4, the relative uncertainties in the band-averaged mean stray-light-correction factors are given for SeaWiFS bands.

Table 5.3: Uncertainties in slit-scatter function model parameters used in Monte Carlo simulations of MOS205 measurements.

Parameter	BSG Uncertainty [%]	RSG Uncertainty [%]
Normalization	2	2
OOB SSF		
m_1	5	3
m_2	5	3
m_3	25	25
Reflection Peak Amplitude P<100		
a_1	5	5

Table 5.4: Relative combined standard uncertainties in the band-averaged L_w stray-light-correction factor for SeaWiFS bands.

SeaWiFS Band	Ratio Corrected/Uncorrected L_W	Uncertainty [%]
1	1.085	0.83
2	1.033	0.36
3	1.012	0.15
4	0.976	0.21
5	0.979	0.58
6	1.014	NOP

a_2

5

5

a_3

5

5

Amplitude (P>100)

a_2

5

5

a_3

5

5

Off CCD Amplitude

10

NOP

5.7 DISCUSSION

The SeaWiFS band-averaged water-leaving radiance stray-light-correction factors measured by MOBY during a two-month deployment (M220) is shown in Fig. 5.36. In Figs. 5.37 and 5.38, the corrected/uncorrected SeaWiFS band-averaged ratios are shown for 4 years of deployments. Each grouping in the figure is a separate deployment. The correction factors have been stable over the entire deployment sequence, implying that the MOBY imaging and the MOS slit-scatter functions, along with the ocean-color, have remained stable over this time frame. The only exception was for the first three deployments of the MOS204 sensor (even buoys, Fig. 5.38), when the Band 1 correction factor was 2 % higher than for the other deployments. For these three deployments, low hydroxyl (OH) optical fiber was used to couple the radiance heads to the instrument bay. This fiber transmitted less light than the other fibers in the blue spectral region, in particular below 400 nm. For these three deployments, then, the relative stray-light contribution to the total signal in the blue spectral region was larger than for subsequent buoys, resulting in the larger Band 1 stray-light-correction factor for these buoys. The observed radiometric stability of the MOBY systems enables us to correct previous deployments for stray light with confidence.
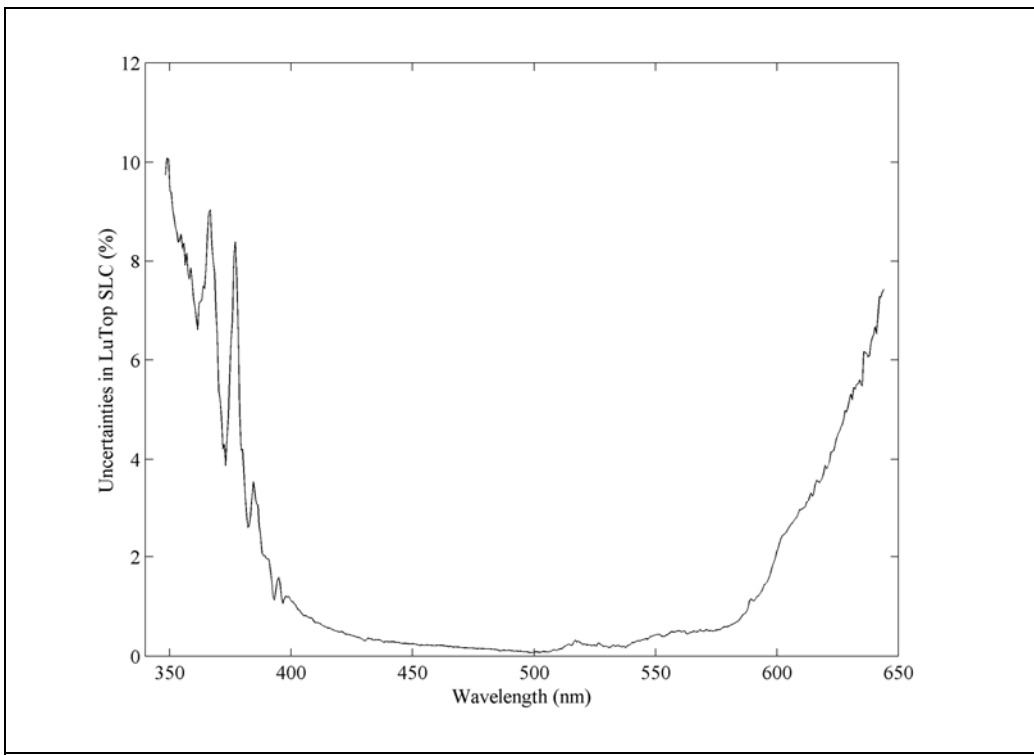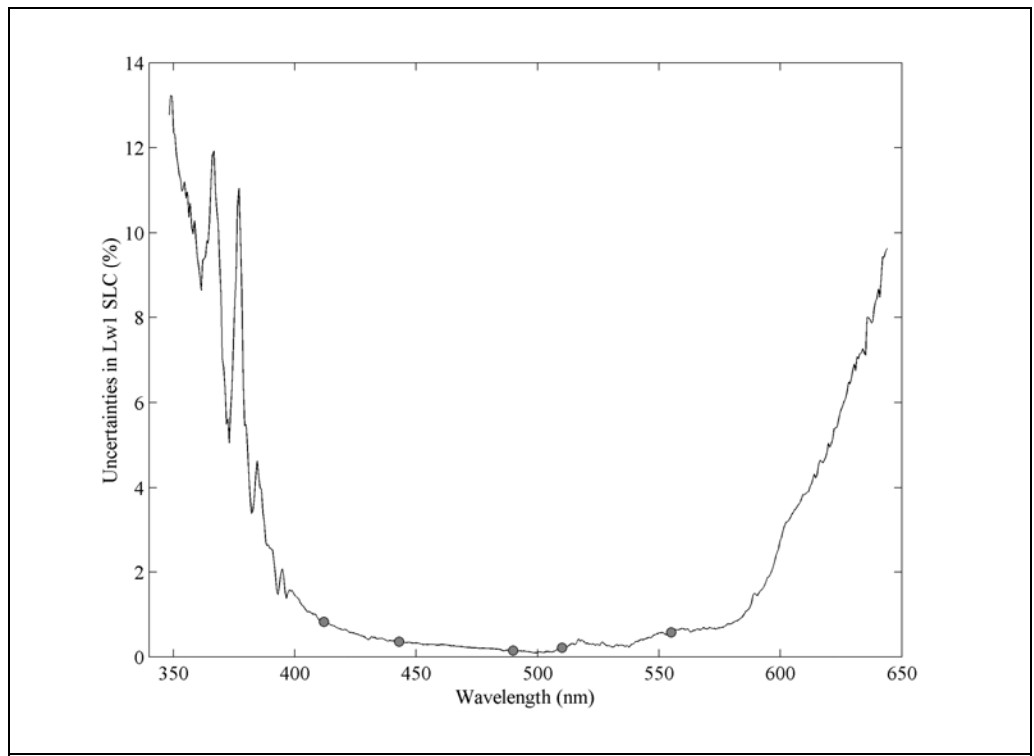
Figure 5.34: Uncertainty in L_u stray-light correction amplitude from Monte Carlo simulation.

5.35: Uncertainty in L_w stray-light correction amplitude from Monte Carlo simulation. Grey circles represent band-center wavelengths of SeaWiFs bands.
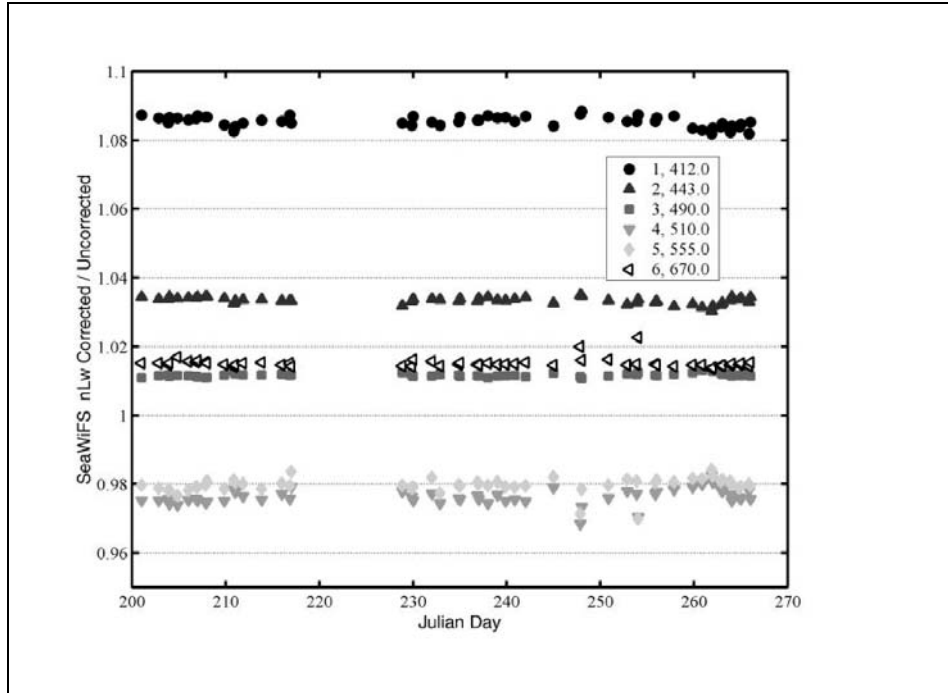
Fig. 5.36: Band-averaged Lw stray-light correction factors for SeaWiFS bands measured by MOBY during deployment 220.
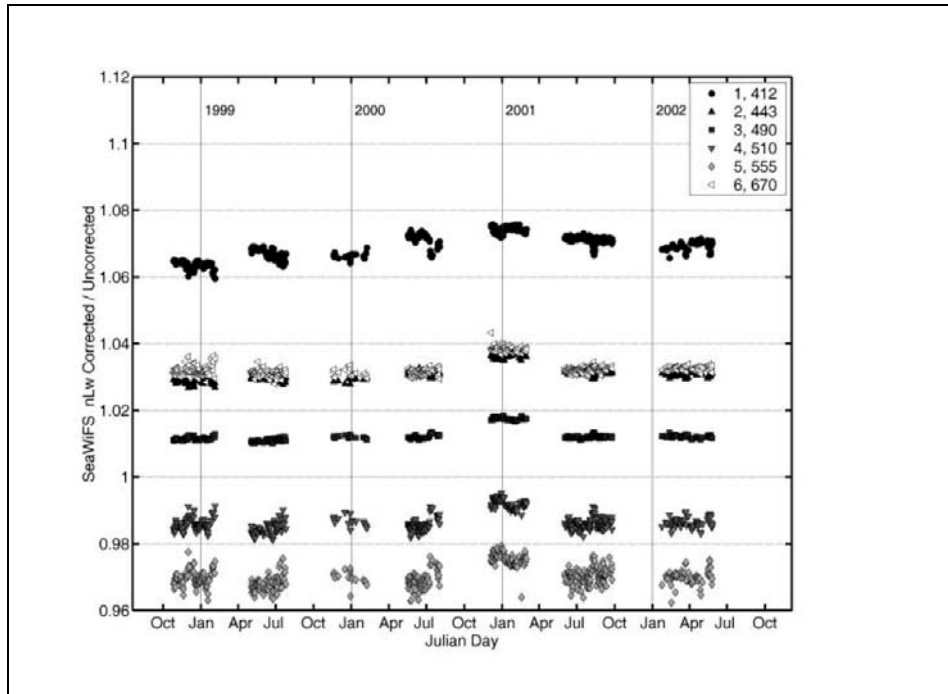

Fig. 5.37: Band-averaged Lw stray-light corrections for SeaWiFS bands measured by odd MOBY buoys from 1998 through 2002.

Impact on SeaWiFS

MOBY is used for the vicarious calibration of SeaWiFS bands 1 through 6 (Barnes *et al.* 2000). Any changes in MOBY-derived water-leaving radiances are directly reflected in SeaWiFS calibration coefficients for these channels. The effect of the MOBY stray-light correction is to increase the water-leaving radiance of SeaWiFS Bands 1 through 4, and decrease the radiance of Bands 5 and 6. SeaWiFS uses the Band 2 (443 nm) to Band 5 (555 nm) ratio to radiometrically determine chlorophyll *a* concentrations in oligotrophic waters (chlorophyll concentrations about 0.3 µg/l); the Band 3 (490 nm) to Band 5 ratio for mesotrophic waters (chlorophyll concentrations ranging from 0.3 µg/l to 1.5 µg/l); and the Band 4 (510 nm) to Band 5 ratio for eutrophic waters (chlorophyll concentrations > 1.5 µg/l) (O'Reilly *et al.* 1998). Correcting for stray light increases the band ratio in oligotrophic waters by 5 % to 6 % and approximately 3.5 % for waters with higher chlorophyll *a* concentrations. The change in band ratios corresponds to a 25 % to 35 % decrease in chlorophyll in oligotrophic waters and a 15 % decrease in mesotrophic and eutrophic waters. The stray-light correction of MOBY reduces global mean chlorophyll a concentrations measured by SeaWiFS by 15 % to 20 %. When combined with additional procedural changes implemented in the 4th reprocessing of the SeaWiFS data set in July 2002 (SeaWiFS 2002), the result was a mean monthly decrease in global chlorophyll a concentration of 6 %. In addition, the stray-light correction greatly reduced the magnitude of an issue with SeaWiFS measuring negative water-leaving radiance in coastal regions with complex aerosol distributions.
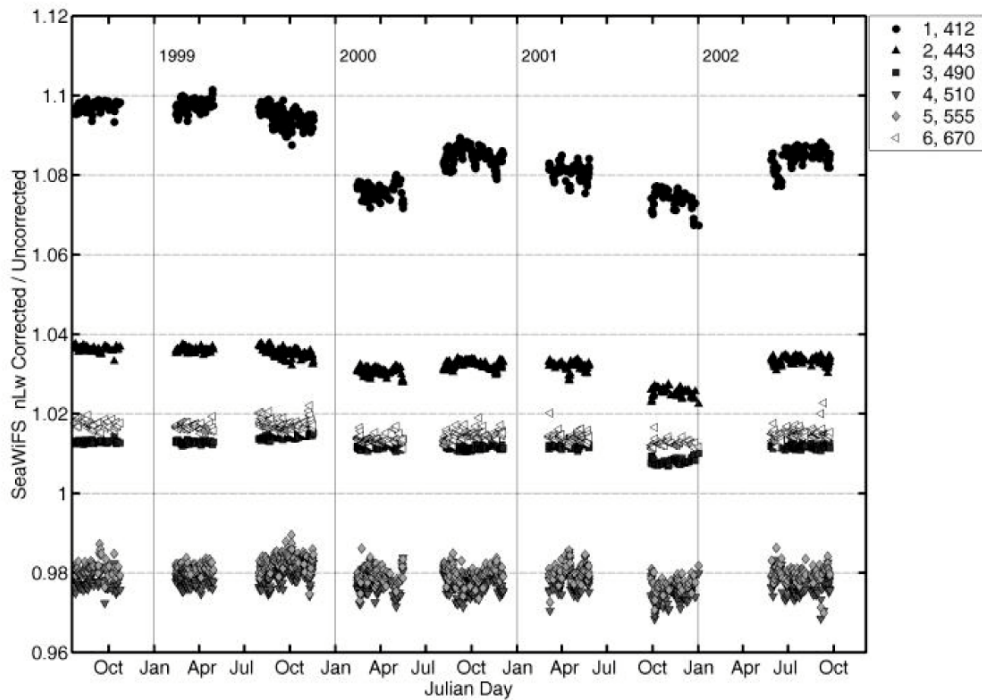

Figure 5.38: Band-averaged L_w stray-light-correction factors for SeaWiFS bands measured by even MOBY buoys from 1998 through 2002.

Implications for algorithm development

The derivation of remote-sensing-based ocean color data products such as chlorophyll *a* involve the integration of measurements by (1) the satellite sensor (*e.g.* SeaWiFS), (2) the vicarious calibration sensors (*e.g.* MOBY), and (3) the instruments used to develop the bio-optical algorithms relating the physical properties of the ocean (*e.g.* chlorophyll a concentration) to a radiometric measurement. Errors in measurements of any one of the three

components of the measurement chain will significantly impact the validity of the final data product. Instruments involved in ocean color measurements are typically calibrated against incandescent sources such as lamp-illuminated integrating spheres or reflectance plaques. These types of calibration sources have very different spectral distributions than the distribution of up-welling or water-leaving radiance and effects of stray light on the instrument response need to be considered for these instruments.

While considerable time and effort can be (and has been) expended to fully characterize and correct a satellite sensor or primary vicarious calibration station for stray light, it is much more difficult to extend the detailed characterization to the myriad instruments used by different groups to develop bio-optical algorithms. No general protocol has been developed to characterize and correct instrumentation used to develop bio-optical algorithms for stray light. However, effects of stray light are effectively canceled when the calibration source distribution approximates a measured ocean color spectrum. We have developed a radiometrically stable, spectrally tunable, solid-state calibration source for ocean color. This unique source approximates the spectral distributions of waters with varying chlorophyll concentrations, and may be used to calibrate, characterize, and to correct instruments' responsivities for stray light.

We have developed the prototype tunable solid-state source using Light Emitting Diodes (LEDs). (Brown *et al*. 2002). The source has 40 different, independently controlled LED channels comprised of 3 to 6 LEDs (depending on their output power) organized into 4 heads that mount onto 5 cm ports in the wall of an integrating sphere. The flux from each channel can be independently changed to model the spectral distribution of water-leaving radiance in different chlorophyll concentration waters. The output is monitored using a reference spectroradiometer integrated into the system. The source is under computer control and is designed to be automatically adjusted to match any desired input target spectrum, within the bandwidth limitations of the individual LEDs (~ 20 nm), to within approximately 5 % over the range from 390 nm to 550 nm.

The source has been tuned to match the water-leaving radiance from blue (oligotrophic), blue-green (mesotrophic), and green (eutrophic) waters, covering a wide range of chlorophyll concentrations. The target spectral distributions and the solid-state source output are shown in Figure 5.39. There is reasonable agreement over most of the spectral range. The sphere radiance is low below 390 nm. This is partially due to the low reflectance of the integrating sphere coating. With a new coating, we expect an order of magnitude increase in the radiance below 400 nm. The source is currently missing diodes at 360 nm, 435 nm, and 455 nm. The radiance around 550 nm is low due to weak diode emission; a problem that is easily addressed with the addition of extra 550 nm LEDs. The source stability and its applicability to the development of stray-light correction algorithms are currently under investigation.

We propose to correct instruments for stray-light errors in water-leaving radiance measurements using a variation on the basic approach developed for SeaWiFS by Wang, *et al*. (2001). Knowing the total spectral responsivity of the SeaWiFS bands, a stray light, or spectral out-of-band correction, is currently applied to each channel based on a semi-analytical water-leaving radiance model developed by Gordon for water with varying chlorophyll a concentrations (Gordon 1995; Wang *et al*. 2001). In this case, we don't know the total spectral responsivity of the instruments. Instead, we used the solid-state source to mimic the varying spectral water-leaving radiance spectral distributions and derive correction factors based on the ratio between the known radiance of the source (as measured by our reference spectroradiometer) and the radiance measured by the ocean color instruments.

5.8 SUMMARY

A simple iterative procedure was developed to correct MOBY measurements for stray light. Several fully operational MOBY systems were characterized *in situ* using a tunable laser-based, fiber-coupled integrating sphere source that was developed and installed at the MOBY field site at University of Hawaii Marine Center, Honolulu, Hawaii for this purpose. MOBY buoys with MOS204 and MOS205 detector systems were characterized and model slit-scatter functions developed. MOBY measurements of a Colored Source validated the stray-light-corrected measurements. In-water MOBY measurements of L_u and L_w were corrected for stray light, and the effect on SeaWiFS bands and derived chlorophyll-a concentrations were evaluated.
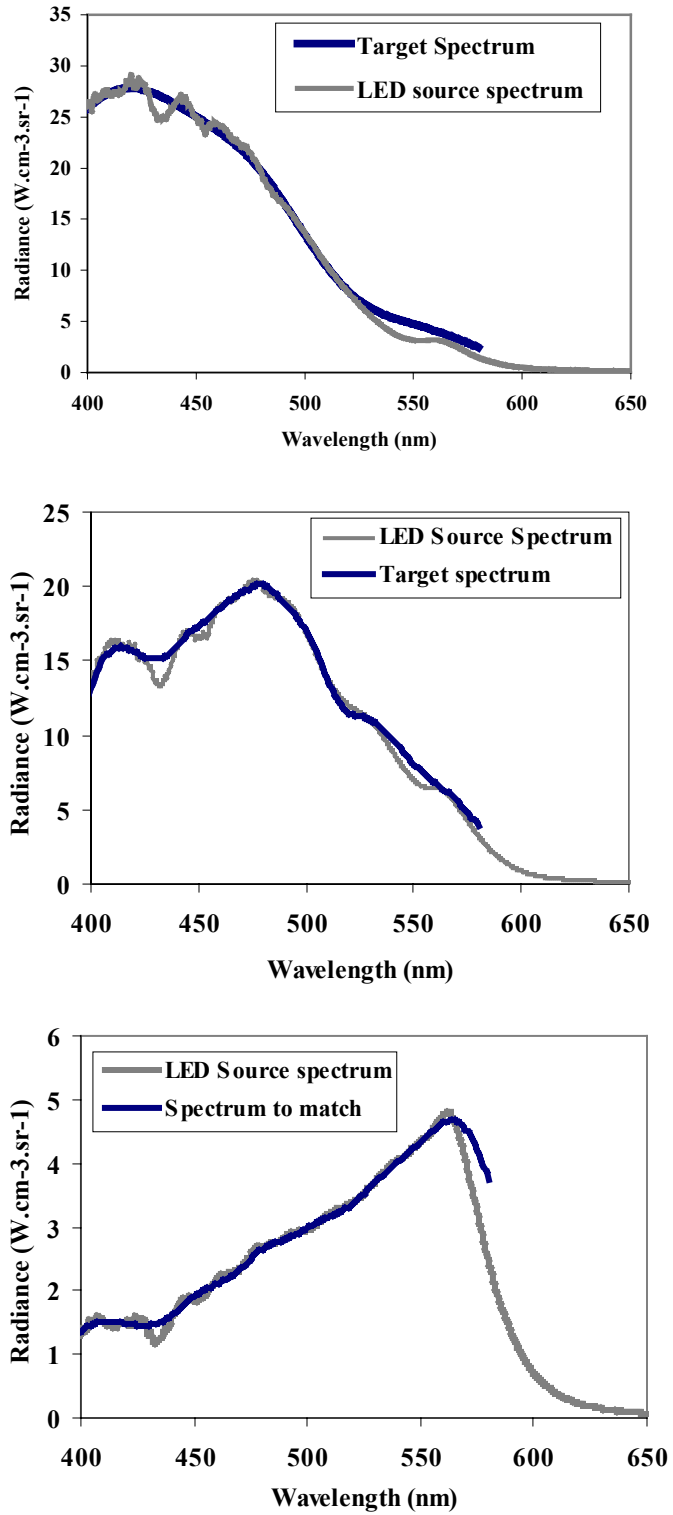
Figure 5.39: Target and LED source spectra for (a) blue, (b) blue-green and (c) green waters.

5.9 ACKNOWLEDGEMENTS

REFERENCES

Barnes, R. A., R. E. Eplee, Jr., W. D. Robinson, G. M. Schmidt, F. S. Patt, S. W. Bailey, M. Wang and C. R. McClain, 2000: The calibration of SeaWiFS on orbit, Proceedings of the SPIE, 4135, 281-293.

Brown, S. W., G. P. Eppeldauer and K. R. Lykke, 2000: NIST facility for spectral irradiance and radiance calibrations with uniform sources, Metrologia, 37, 579-582.

Brown, S. W. and Y. Ohno, 1999: NIST calibration facility for display colorimeters, Proc. SPIE, 3636, 162-169.

Brown, S. W., C. Santana and G. P. Eppeldauer, 2002: Development of a tunable LED-based colorimetric source, J. Res. Natl. Inst. Stand. Technol., 107, 363-371.

Butler, J. J., B. C. Johnson, S. W. Brown, H. W. Yoon, R. A. Barnes, B. L. Markham, S. F. Biggar, E. F. Zalewski, P. R. Spyak, J. W. Cooper and F. Sakuma, 1999: Radiometric measurement comparisons using transfer radiometers in support of the calibration of NASA's Earth Observing System (EOS) sensors. Sensors, Systems, and Next-Generation Satellites III. P. N. Slater. Bellingham, WA, Society of Photo-Optical Instrumentation Engineers. 3870: 180-192.

Clark, D. K., M. E. Feinholz, M. A. Yarbrough, B. C. Johnson, S. W. Brown, Y. S. Kim and R. A. Barnes, 2002a: Overview of the radiometric calibration of MOBY, Proceedings of the SPIE, 4483, 64-76.

Clark, D. K., H. R. Gordon, K. Voss, Y. Ge, W. Broenkow and C. Trees, 1997: Validation of atmospheric correction over the oceans, Journal of Geophysical Research, 102, 17209-17217.

Clark, D. K., M. A. Yarbrough, M. E. Feinholz, S. Flora, W. Broenkow, Y. S. Kim, B. C. Johnson, S. W. Brown, M. Yuen and J. L. Mueller, 2002b: MOBY, a radiometric buoy for performance monitoring and vicarious calibration of satellite ocean color sensors: Measurement and data analysis protocols. Ocean Optics Protocols for Satellite Ocean Color Sensor Validation, Rev. 3. J. L. M. a. G. S. Fargion. Greenbelt, MD, NASA/TM-2002-210004/Rev3-Vol2. 2.

Deschamps, P. Y., F. M. Breon, M. Leroy, A. Podaire, A. Bricaud, J. C. Buriez and G. Seze, 1994: The POLDER mission: instrument characteristics and scientific objectives, IEEE Trans. Geosci. Remote Sens, 32, 598-615.

Eppeldauer, G. P. and D. C. Lynch, 2000: Opto-mechanical and electronic design of a tunnel-trap Si- radiometer, J. Res. NIST, 105(6), 813-828.

Esaias, W. E., M. R. Abbott, I. Barton, O. B. Brown, J. W. Campbell, K. L. Carder, D. K. Clark, R. H. Evans, F. E. Hoge, H. R. Gordon, W. M. Balch, R. Letelier and P. J. Minnett, 1998: An overview of MODIS capabilities for ocean science observations, IEEE Trans. Geosci. Remote Sens, 36, 1250-1265.

Gordon, H. R., 1995: Remote sensing of ocean color: a methodology for dealing with broad spectral bands and significant out-of-band response, Appl. Optics, 34, 8363-8374.

Gordon, H. R., 1998: In-orbit calibration strategy for ocean color sensors, Remote Sens. Environ., 63, 265-278.

Habauzit, C., S. W. Brown, K. R. Lykke, B. C. Johnson, M. E. Feinholz, M. A. Yarbrough and D. K. Clark, 2003: Radiometric characterization and absolute calibration of the Marine Optical System (MOS) bench unit, Journal of Atmospheric and Oceanic Technology, 20(3), 383-391.

Hooker, S. B., C. R. McClain and A. W. Holmes, 1993: Ocean color imaging: CZCS to SeaWiFS, Marine Tech. Soc. Journal, 27, 3-15.

Isaacman, A., B. Franz and R. E. J. Eplee, 1999: An investigation of time variability in water-leaving radiances retrieved from ocean color measurements. ALPS99 Conference, Meribel, France.

Kostkowski, H. J., 1979: The relative spectral responsivity and slit-scatter function of a spectroradiometer. Self Study Manual on Optical Radiation Measurements, NBS Tech. Note 910-4. F. E. Nicodemus. Washington, DC, U.S. Department of Commerce: 1-34.

Mueller, J. (2002). personal communication.

O'Reilly, J. E., S. Maritorena, B. G. Mitchell, D. A. Siegel, K. L. Carder, S. A. Garver, M. Kahru and C. McClain, 1998: Ocean color chloropohyll algorithms for SeaWiFS, Journal of Geophysical Research, 103, 24937-24953.

SeaWiFS (2002). http://seawifs.gsfc.nasa.gov/SEAWIFS/RECAL/Repro4/.

Shumaker, J. B., 1979: Deconvolution. Self Study Manualon Optical Radiation Measurements, NBS Tech. Note 910-4. F. E. Nicodemus. Washington, DC, U.S. Department of Commerce: 35-90.

Walker, J. H., R. D. Saunders and A. T. Hattenburg, 1987: Spectral Radiance Calibrations, NBS Special Publication 250-1. Washington, DC, U.S. Government Printing Office.

Wang, M., A. A. Isaacman, B. A. Franz and C. R. McClain, 2002: Ocean-color optical property data derived from the Japanese Ocean Color and Temperature Scanner and the French Polarization and Directionality of the Earth's Reflectances: a comparison study, Appl. Optics, 41, 974-990.

Wang, M., B. A. Franz, R. A. Barnes and C. R. McClain, 2001: Effects of spectral bandpass on SeaWiFS-retrieved near-surface optical properties of the ocean, Appl. Optics, 40, 343-348.